

FILT3R: Latent State Adaptive Kalman Filter for Streaming 3D Reconstruction

Seonghyun Jin¹ and Jong Chul Ye^{1*}

KAIST AI

jinotter3@kaist.ac.kr, jong.ye@kaist.ac.kr

Abstract. Streaming 3D reconstruction maintains a persistent latent state that is updated online from incoming frames, enabling constant-memory inference. A key failure mode is the state update rule: aggressive overwrites forget useful history, while conservative updates fail to track new evidence, and both behaviors become unstable beyond the training horizon. To address this challenge, we propose **FILT3R**, a training-free latent filtering layer that casts recurrent state updates as stochastic state estimation in token space. FILT3R maintains a per-token variance and computes a Kalman-style gain that adaptively balances memory retention against new observations. Process noise – governing how much the latent state is expected to change between frames – is estimated online from EMA-normalized temporal drift of candidate tokens. Using extensive experiments, we demonstrate that FILT3R yields an interpretable, plug-in update rule that generalizes common overwrite and gating policies as special cases. Specifically, we show that gains shrink in stable regimes as uncertainty contracts with accumulated evidence, and rise when genuine scene change increases process uncertainty, improving long-horizon stability for depth, pose, and 3D reconstruction, compared to the existing methods. Code will be released at <https://github.com/jinotter3/FILT3R>.

Keywords: Streaming 3D Reconstruction · State Estimation · Kalman Filtering · Length Generalization

* Corresponding author.

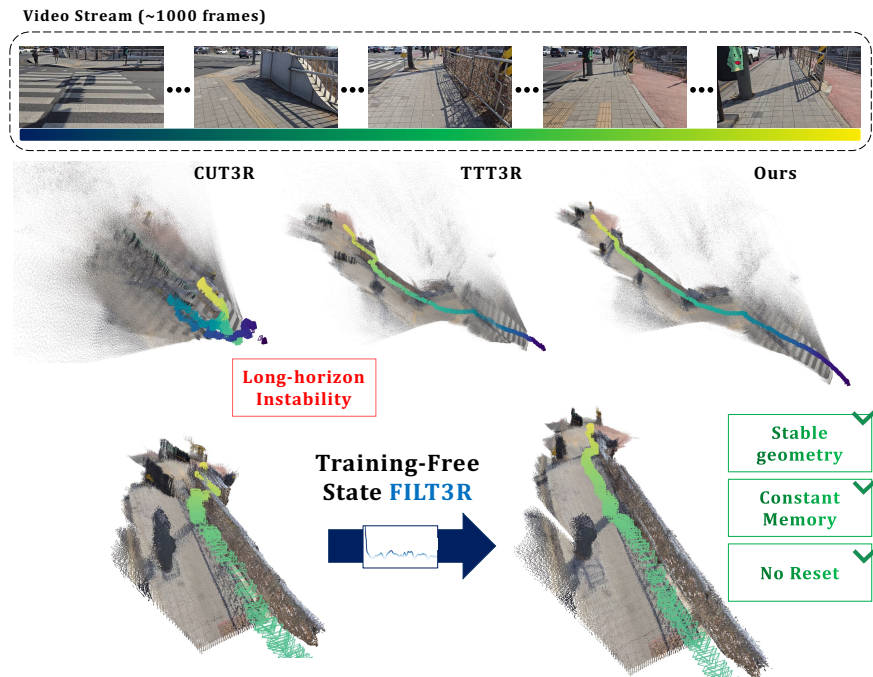


Fig. 1: FILT3R enables stable long-horizon streaming 3D reconstruction without resets. Top: dense input frames from a long video stream. Middle: final reconstructions from the same frozen streaming backbone under different latent-state update rules. Uniform overwrite (CUT3R) and heuristic gating (TTT3R) accumulate drift and/or forget previously integrated evidence, leading to long-horizon instability and degraded geometry. Bottom: a zoom-in around frames beyond 600 highlights that FILT3R preserves stable geometry over long rollouts. Trajectory colors indicate time.

1 Introduction

Streaming 3D reconstruction aims to predict geometry and camera motion from an image stream while using constant memory and low latency. Recent recurrent architectures achieve this by maintaining a compact set of persistent latent tokens, which distill the scene’s context and evolve dynamically as new frames arrive [32]. In practice, performance often degrades when the sequence length exceeds the training horizon: small update biases accumulate into drift, and the latent state gradually loses information that is no longer supported by the most recent frame. Since a new candidate latent state should be estimated from the current frame and the previous state, the system must then decide how much to trust the candidate (fast adaptation) versus the previous state (long-term consistency).

Existing streaming update rules are mostly manually engineered to manage this trade-off. Uniform overwrites (*e.g.*, CUT3R [32]) always trust the new can-

didate, which can lead to catastrophic forgetting. While training-free gates based on attention statistics (*e.g.*, TTT3R [4]) improve stability, they remain largely heuristic; they scale updates without an explicit representation of uncertainty or a principled mechanism for adaptation as confidence increases. Mathematically, existing streaming updates can be written as $\mathbf{s}_t = (1 - \beta_t) \odot \mathbf{s}_{t-1} + \beta_t \odot \tilde{\mathbf{s}}_t$, where $\beta_t \in [0, 1]^N$ determines how quickly past evidence is forgotten. Uniform overwrite ($\beta_t = \mathbf{1}$) yields a one-step memory, while fixed-gain gates impose a constant forgetting half-life regardless of stream stability.

Inspired by this formulation, we argue that the recurrent state in streaming reconstruction is naturally a *belief state*, and that the candidate state produced by the decoder is a noisy *measurement* of that belief. This viewpoint leads directly to our novel adaptive filtering formulation, which we call **FILT3R**. In particular, FILT3R formulates the state update as a Kalman-style interpolation whose gain is governed by two uncertainties: (i) *process noise*—how much the underlying scene latent is expected to change between frames—and (ii) *measurement noise*—how reliable the decoder’s current prediction is. Specifically, FILT3R adopts an adaptive Kalman filtering (AKF) framework [15] with a fixed measurement model. Adaptivity is centered on the process model, allowing Kalman gains to attenuate as tokens gain confidence during stable periods – thereby extending the effective memory horizon – and increase in response to process noise that indicates a genuine scene change. More specifically, FILT3R uses a *fixed* scalar measurement noise r and estimates only the *process noise* adaptively from temporal drift in the latent space. This formulation not only reduces computational complexity but also circumvents a critical failure mode, as validated by our empirical findings.

Our contribution can be summarized as follows:

- (i) We recast streaming 3D reconstruction as stochastic state estimation in latent token space, and introduce **FILT3R**, an adaptive latent filtering layer for streaming 3D reconstruction.
- (ii) FILT3R is a training-free, lightweight, and interpretable plug-and-play filtering approach with adaptive process noise estimated from internal model signals and fixed measurement noise, following the classical AKF paradigm.
- (iii) We provide extensive evaluation across short- and long-horizon streaming depth, pose, and reconstruction settings, and analyze how uncertainty-aware gains improve length generalization. The results confirm that FILT3R consistently outperforms prior streaming baselines and improves long-horizon stability across metrics.

2 Related Work

Streaming and recurrent 3D reconstruction. Classical and learning-based 3D streaming pipelines have progressed from short-horizon depth/pose models to online recurrent reconstruction. Representative geometric estimators include RAFT-style correlation, DeepV2D, and DROID-SLAM [25–27]. For online scene understanding, methods such as iMAP, NICE-SLAM, Co-SLAM, Point-SLAM, and

MASt3R-SLAM maintain a persistent latent map updated as frames arrive [16, 18, 23, 30, 39]. Recent foundation-style 3D models further improve feed-forward reconstruction quality, from DUST3R/MASt3R to larger multi-view architectures including VGGT and its follow-ups [5, 11, 13, 20, 31, 33, 34, 36]. Streaming variants such as Spann3R, CUT3R, SLAM3R, Point3R, Stream3R, StreamVGGT, and WinT3R explicitly target long-horizon online inference under bounded memory [10, 12, 14, 29, 32, 35, 40].

A central design choice is the state update rule in recurrent memories. CUT3R uses uniform overwrite [32], while recent training-free methods introduce adaptive gating signals from attention or motion cues, including TTT3R, TTSA3R, and MUT3R [4, 19, 38]. In parallel, test-time adaptation methods update model parameters online, *e.g.*, test-time training and entropy minimization [24, 28].

In streaming 3D reconstruction, errors compound with rollout length, causing drift and forgetting beyond the training horizon. This failure mode is visible in overwrite-based and heuristic-gated recurrent updates [4, 32, 38]. Our goal is to address this by explicitly propagating uncertainty so gains decay in stable periods and rise only when estimated process uncertainty indicates genuine scene change.

Uncertainty estimation and filtering. Kalman filtering provides a principled framework for sequential estimation under linear-Gaussian assumptions [8]. Adaptive Kalman filtering estimates noise covariances online when dynamics are non-stationary [15]. Neural and differentiable variants include Deep Kalman Filters and Backprop KF [7, 9]. We adopt this perspective for latent token memories, using adaptive process noise and propagated uncertainty to derive per-token gains while keeping measurement noise fixed.

3 FILT3R

3.1 Problem formulation

We consider a recurrent streaming reconstruction model that maintains persistent state tokens $\mathbf{s}_t \in \mathbb{R}^{N \times D}$ and, given an incoming frame at time t , produces a candidate state token $\tilde{\mathbf{s}}_t \in \mathbb{R}^{N \times D}$ using a decoder that attends to image tokens and the previous state [32]. Here, N and D refer to the number of tokens and token dimension, respectively.

Specifically, we interpret \mathbf{s}_t as a *belief* over the scene latent at time t and $\tilde{\mathbf{s}}_t$ as a noisy *measurement* of that belief produced by the decoder. This suggests modeling the dynamics with a stochastic state-space model in token space:

$$\mathbf{s}_t = \mathbf{s}_{t-1} + \mathbf{w}_t, \quad \mathbf{w}_t \sim \mathcal{N}(\mathbf{0}, \mathbf{Q}_t), \quad (1)$$

$$\tilde{\mathbf{s}}_t = \mathbf{s}_t + \mathbf{v}_t, \quad \mathbf{v}_t \sim \mathcal{N}(\mathbf{0}, \mathbf{R}), \quad (2)$$

where \mathbf{Q}_t models uncertainty in latent evolution (process noise) and \mathbf{R} models uncertainty in the decoder’s prediction (measurement noise).

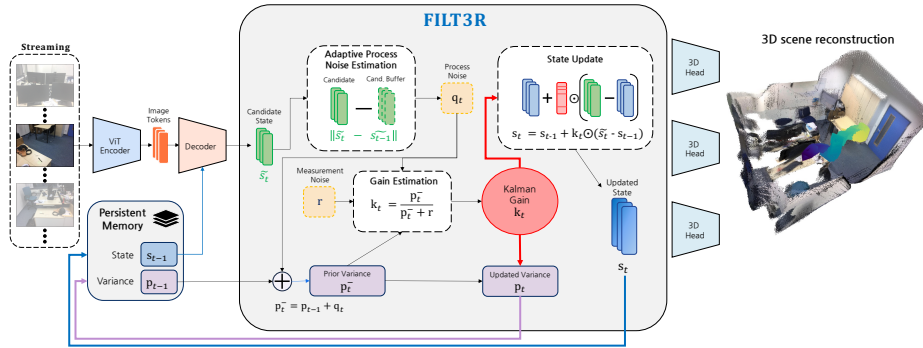


Fig. 2: FILT3R overview. The persistent memory s_{t-1} is fused with the decoder’s candidate \tilde{s}_t via a token-wise Kalman gain k_t . Process noise q_t is estimated adaptively from EMA-normalized temporal drift, while measurement noise r is a scalar hyperparameter shared across tokens. Variance p_t is propagated across time steps, enabling gains that naturally shrink in stable regimes and increase during scene change.

Streaming video is non-stationary: the scene can change rapidly during motion and remain static during pauses. We therefore adopt an *adaptive Kalman filtering* (AKF) approach [15], estimating process noise Q_t online from the model’s internal representations.

A key design choice in FILT3R is to keep measurement noise *fixed* using a single scalar shared across tokens, *i.e.* $R = rI$. The rationale is that the decoder is a frozen pretrained network: its prediction quality is determined by its architecture and training, not by the current scene dynamics. In classical AKF, this corresponds to the standard assumption that the sensor noise is known [15].

In contrast, we found that making both Q_t and R_t adaptive introduces the risk of correlated noise estimates: scene transitions simultaneously increase temporal drift (which feeds Q_t) and attention novelty (which would feed R_t). When both spike together, the gain k_t can overshoot, producing the same instability that heuristic gates suffer from. A fixed r in our FILT3R provides a stable anchor, and all adaptivity enters through the process noise.

3.2 Update rule

We assume a diagonal per-token variance $p_t \in \mathbb{R}^N$ (one scalar per token), approximating each token’s covariance as isotropic. Equivalently, we use diagonal covariance approximations $Q_t = \text{diag}(q_t)$ and $P_t = \text{diag}(p_t)$, which yields elementwise Kalman updates. Then, the variance prediction follows the standard Kalman prediction step:

$$p_t^- = p_{t-1} + q_t, \quad (3)$$

where $\mathbf{q}_t \in \mathbb{R}^N$ is the per-token process noise estimated online (Sec. 3.2), and the Kalman gain is given by

$$\mathbf{k}_t = \frac{\mathbf{p}_t^-}{\mathbf{p}_t^- + r}, \quad (4)$$

Consequently, the state update according to AKF is a gain-weighted interpolation:

$$\mathbf{s}_t = \mathbf{s}_{t-1} + \mathbf{k}_t \odot (\tilde{\mathbf{s}}_t - \mathbf{s}_{t-1}). \quad (5)$$

and the variance is updated using the scalar Joseph form:

$$\mathbf{p}_t = (\mathbf{1} - \mathbf{k}_t)^2 \odot \mathbf{p}_t^- + r\mathbf{k}_t^2. \quad (6)$$

where \odot refers to the Hadamard product, and $\mathbf{k}_t^2 = \mathbf{k}_t \odot \mathbf{k}_t$.

Uncertainty modeling of latent evolution. Given the update rules for $\mathbf{s}_t, \mathbf{p}_t$, AKF formulation requires the process noise variance that captures how much the scene latent is expected to change between frames. In a static scene, \mathbf{q}_t should be small; during rapid motion or scene transitions, \mathbf{q}_t should be large. FILT3R estimates this from the temporal drift of consecutive candidate states, using a per-stream EMA baseline to calibrate the scale.

Specifically, we model the i -th token process noise through a sigmoid gate:

$$q_{t,i} = q_{\min} + (q_{\max} - q_{\min}) \cdot \sigma(\alpha_q(g_{t,i} - \tau_q)), \quad (7)$$

where q_{\min}, q_{\max} bound the process noise, α_q controls the sharpness of the transition, and τ_q is the midpoint, and $g_{t,i}$ refers to the normalized drift score with respect to the running EMA baseline of the stream-level mean drift $\hat{\Delta}_t$:

$$g_{t,i} = \Delta_{t,i} / \hat{\Delta}_t \quad (8)$$

$$\hat{\Delta}_t = (1 - \lambda_\Delta) \hat{\Delta}_{t-1} + \lambda_\Delta \bar{\Delta}_t, \quad (9)$$

where λ_Δ is the EMA rate and

$$\bar{\Delta}_t := \sum_i \Delta_{t,i} / N, \quad \text{where } \Delta_{t,i} = \|\tilde{\mathbf{s}}_{t,i} - \tilde{\mathbf{s}}_{t-1,i}\|_2. \quad (10)$$

The normalized drift score measures whether the current drift is high or low relative to the stream's running baseline.

Intuitively, when the drift is typical (near the EMA baseline), the sigmoid is near its midpoint and $q_{t,i}$ takes a moderate value; when the drift is unusually large, $q_{t,i}$ approaches q_{\max} , signaling rapid scene change; when the drift is small, $q_{t,i}$ approaches q_{\min} , indicating stability.

Implementation issue. For numerical stability, we add small ϵ to the denominators of (4) and (8) to avoid the division by a near zero value. The gain in (4) is additionally clamped to $[k_{\min}, k_{\max}]$ to prevent complete freezing or full overwrite. Similarly, the EMA baseline is clamped to a floor Δ_{floor} to avoid division instability.

The overhead of our AKF formulation is minimal: one N -dimensional vector of token variances, one per-stream EMA scalar for normalizing temporal drift, and one $N \times D$ buffer for the previous candidate.

3.3 Filtering as adaptive token retention

The Kalman gain \mathbf{k}_t in Eq. (5) acts as a per-token update coefficient $\beta_t := \mathbf{k}_t \in [0, 1]^N$, yielding an exponential-smoothing form $\mathbf{s}_t = (1 - \beta_t) \odot \mathbf{s}_{t-1} + \beta_t \odot \tilde{\mathbf{s}}_t$. Unlike overwrite ($\beta_t \equiv \mathbf{1}$) or fixed/heuristic gates, FILT3R propagates uncertainty (Eqs. (3) and (6)), so gains *naturally shrink* as the state becomes confident in stable regimes, extending the effective memory horizon, while still producing gain increases when inferred process noise favors adaptation.

More specifically, the Kalman gain (Eq. (4)) is entirely driven by the ratio $\mathbf{p}_t^- / (\mathbf{p}_t^- + r)$. In stable regimes, \mathbf{q}_t stays near q_{\min} , so \mathbf{p}_t^- gradually decreases as the Joseph update (Eq. (6)) shrinks the variance, causing \mathbf{k}_t to decay and the effective memory horizon to grow. During scene transitions, \mathbf{q}_t spikes, \mathbf{p}_t^- increases, and \mathbf{k}_t rises, allowing the filter to rapidly integrate new evidence. With \mathbf{q}_t driving \mathbf{p}_t^- , the gain in Eq. (4) increases under large drift and decreases as uncertainty contracts in stable regimes.

This formulation clarifies the relationship to prior update rules:

- *Uniform overwrite* (CUT3R): $\beta_t \equiv \mathbf{1}$. Equivalent to $r = 0$ (infinite trust in the measurement).
- *Heuristic gates* (TTT3R): β_t computed from instantaneous attention/change statistics without uncertainty propagation. Equivalent to resetting variance to a constant each step.
- *Fixed interpolation*: $\beta_t \equiv \beta$. A single point on the steady-state q/r curve (see Appendix A.1).

In fact, in FILT3R, β_t is derived via recursive uncertainty updates (Eqs. (3), (4) and (6)). This yields Kalman gains that decay at a rate of $\mathcal{O}(1/t)$ in static scenes (see Appendix A.1, Prop. 1) but spike in response to process noise signaling a scene change. To support this mechanism, Appendix A.1 provides a formal unrolling demonstrating that the effective memory horizon expands as evidence accumulates. It further includes a rigorous proof of the $1/t$ gain decay in static environments and a proposition establishing the relationship between the steady-state gain and the noise ratio q/r .

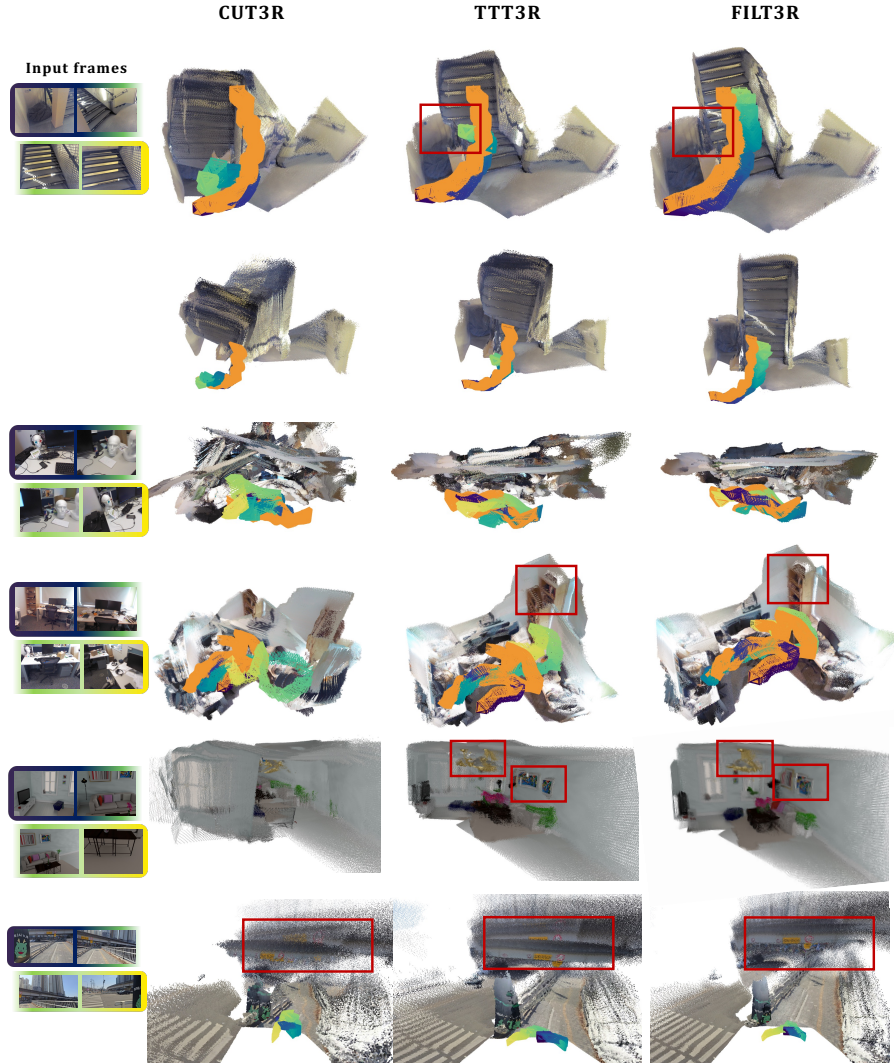


Fig. 3: Qualitative long-horizon streaming 3D reconstruction. CUT3R often suffers from catastrophic forgetting and drift, while TTT3R reduces but does not eliminate long-horizon instability, leading to fragmented surfaces and inconsistent revisited regions (red boxes). FILT3R produces more coherent geometry over long rollouts. Ground-truth trajectory is shown in orange; the predicted trajectory is color-coded by time.

4 Experiments

4.1 Setup

Model and update rules. We evaluate FILT3R as a drop-in replacement for the state update in a CUT3R-style recurrent architecture [32]. All methods share identical backbone weights; only the online update policy differs. FILT3R uses the token-wise filtering update in Eq. (5) with adaptive process noise Eq. (7) and gain computation in Eq. (4).

Tasks and metrics. We report (i) video depth estimation with Abs Rel, $\delta < 1.25$, and log RMSE, (ii) camera pose estimation with ATE, RPE-translation, and RPE-rotation, and (iii) 3D reconstruction with Accuracy, Completeness, and Normal Consistency. For depth, we report both metric-scale and per-sequence scale-aligned metrics following common practice. For long-horizon benchmarks, we additionally visualize error versus sequence length to characterize drift.

Datasets. Short-horizon depth is evaluated on Sintel [2], Bonn [17], and KITTI [6] following prior protocols. Long-horizon behavior is evaluated on extended TUM [22] and Bonn [17] sequences substantially longer than the training horizon. 3D reconstruction quality is measured on 7-Scenes [21] and NRGBD [1]. Full dataset and preprocessing details are provided in the appendix.

Baselines. We compare against CUT3R [32] (uniform overwrite) and TTT3R [4] (heuristic confidence scaling). We additionally report streaming reconstruction baseline with an explicit spatial memory architecture (Point3R). Additional comparisons with TTT3R+Reset are provided in Appendix 8 and Appendix 9.

Hyperparameter selection protocol. FILT3R has a small set of scalar hyperparameters controlling process and measurement noise. To avoid per-benchmark tuning, we tune on a held-out development set (long-horizon TUM-200 for pose, and a short-horizon set for depth) and use the same hyperparameters across all the experiments. The list of hyperparameters is provided in the appendix.

Origin-aligned ATE. Standard ATE applies a global alignment over the full trajectory, which can partially mask progressive drift. We therefore also report ATE_{orig} , aligning only the first frame and evaluating the remaining trajectory without further alignment, so drift accumulation is directly reflected in the error.

4.2 Long-horizon 3D reconstruction

Table 1 reports 3D reconstruction quality on 7-Scenes and NRGBD at long sequence lengths. On 7-Scenes, FILT3R consistently outperforms CUT3R and TTT3R, with the gap widening as sequences lengthen: mean accuracy improves from 0.040 to 0.020 at length 300 and from 0.066 to 0.024 at length 500 compared to TTT3R, while maintaining strong completeness and normal consistency. At

Table 1: 3D reconstruction on 7-Scenes and NRGBD. Accuracy (Acc), Completeness (Comp), and Normal Consistency (NC); Mean and Median (Med.) are reported. Point3R runs out of memory (OOM) at length 1000.

(a) **7-Scenes** (lengths 300 / 500 / 1000)

Method	Length 300						Length 500						Length 1000					
	Acc↓		Comp↓		NC↑		Acc↓		Comp↓		NC↑		Acc↓		Comp↓		NC↑	
	Mean	Med.																
CUT3R	0.134	0.090	0.076	0.041	0.544	0.565	0.183	0.133	0.093	0.036	0.530	0.544	0.233	0.170	0.101	0.017	0.511	0.515
Point3R	0.045	0.025	0.032	0.013	0.564	0.598	0.057	0.026	0.025	0.008	0.556	0.584	OOM					
TTT3R	0.040	0.025	0.024	0.005	0.566	0.602	0.066	0.038	0.032	0.006	0.551	0.576	0.145	0.092	0.051	0.010	0.525	0.536
FILT3R (ours)	0.020	0.009	0.022	0.004	0.568	0.603	0.024	0.011	0.023	0.004	0.559	0.589	0.054	0.028	0.028	0.005	0.535	0.550

(b) **NRGBD** (lengths 300 / 400 / 500)

Method	Length 300						Length 400						Length 500					
	Acc↓		Comp↓		NC↑		Acc↓		Comp↓		NC↑		Acc↓		Comp↓		NC↑	
	Mean	Med.																
CUT3R	0.216	0.122	0.073	0.017	0.583	0.629	0.293	0.212	0.103	0.042	0.561	0.592	0.313	0.238	0.141	0.045	0.558	0.585
Point3R	0.065	0.037	0.012	0.003	0.617	0.693	0.084	0.040	0.020	0.003	0.613	0.684	0.112	0.046	0.028	0.003	0.614	0.687
TTT3R	0.102	0.044	0.024	0.004	0.613	0.684	0.144	0.064	0.072	0.011	0.598	0.656	0.170	0.095	0.090	0.019	0.590	0.642
FILT3R (ours)	0.079	0.027	0.012	0.004	0.628	0.710	0.086	0.036	0.026	0.005	0.623	0.701	0.096	0.042	0.035	0.005	0.621	0.697

Table 2: Long-horizon camera pose on TUM-RGBD. We report standard ATE (with global Procrustes alignment) and origin-aligned ATE (ATE_{orig}), which aligns only the first frame and therefore exposes progressive drift. FILT3R provides clear long-horizon stability gains.

Method	TUM-400				TUM-600				TUM-800			
	ATE↓	$ATE_{\text{orig}}↓$	RPE-t↓	RPE-r↓	ATE↓	$ATE_{\text{orig}}↓$	RPE-t↓	RPE-r↓	ATE↓	$ATE_{\text{orig}}↓$	RPE-t↓	RPE-r↓
CUT3R	0.109	0.302	0.010	0.381	0.145	0.425	0.008	0.430	0.173	0.493	0.008	0.486
TTT3R	0.055	0.128	0.010	0.328	0.084	0.176	0.009	0.365	0.097	0.214	0.009	0.387
FILT3R (ours)	0.033	0.074	0.009	0.305	0.042	0.082	0.009	0.332	0.057	0.107	0.009	0.362

length 1000—well beyond the training horizon—Point3R runs out of memory, while CUT3R and TTT3R degrade substantially; FILT3R continues to produce coherent geometry, confirming that uncertainty propagation compounds in value over long rollouts. On NRGBD, FILT3R improves over CUT3R and TTT3R at all lengths and remains competitive with prior streaming baselines at shorter horizons.

4.3 Long-horizon camera pose estimation

As shown in Table 2, FILT3R substantially reduces long-horizon trajectory error on extended TUM-RGBD sequences. The improvements are most pronounced under origin-aligned ATE, which directly exposes progressive drift: at 800 frames, ATE_{orig} drops from 0.214 (TTT3R) and 0.493 (CUT3R) to 0.107 with FILT3R. Standard ATE also improves (0.097 \rightarrow 0.057 at 800 frames). Local relative errors are similar to TTT3R in translation (RPE-t \approx 0.009), while rotation error decreases (0.387 \rightarrow 0.362 at 800 frames), suggesting FILT3R primarily mitigates slow drift and catastrophic forgetting rather than short-term relative motion.

4.4 Long-horizon video depth estimation

Table 3: Long-horizon video depth on Bonn (metric scale). Sequences are truncated to the indicated length. FILT3R maintains stable metric depth predictions as sequence length grows, whereas competing methods suffer from accumulating drift.

Method	Bonn-300			Bonn-400			Bonn-500		
	Abs Rel↓	$\delta < 1.25$ ↑	log RMSE↓	Abs Rel↓	$\delta < 1.25$ ↑	log RMSE↓	Abs Rel↓	$\delta < 1.25$ ↑	log RMSE↓
CUT3R	0.107	88.7	0.162	0.107	89.6	0.161	0.101	90.6	0.156
TTT3R	0.108	90.1	0.163	0.104	91.2	0.158	0.100	92.1	0.154
FILT3R (ours)	0.093	93.8	0.152	0.090	94.1	0.149	0.089	94.4	0.148

Table 3 evaluates metric-scale depth on extended Bonn sequences (300–500 frames), beyond the training horizon. FILT3R achieves the best performance at every truncation length. Compared to TTT3R, FILT3R reduces Abs Rel from 0.108 to 0.093 at 300 frames and from 0.100 to 0.089 at 500 frames, while improving $\delta < 1.25$ from 90.1 to 93.8 and from 92.1 to 94.4. The consistently lower log RMSE indicates improved robustness to rare but severe outlier predictions that can arise from overwriting a stable latent state with a noisy candidate update. Figure 4 (bottom) further shows FILT3R maintains lower error across sequence prefixes, indicating reduced drift accumulation.

4.5 Short-horizon regression check

Finally, we verify that FILT3R does not sacrifice short-horizon accuracy for long-horizon stability. Table 4 compares the three update rules under identical backbone weights. FILT3R matches or improves short-horizon accuracy, while providing clear long-horizon stability gains. Under metric-scale evaluation the gains are larger: Abs Rel drops from 1.029 (CUT3R) and 0.977 (TTT3R) to 0.772 on Sintel, and from 0.103 / 0.090 to 0.067 on Bonn. Full comparisons including optimization-based and full-attention baselines are in Appendix E.

4.6 Efficiency

Table 5 and Figure 5 compare runtime and memory. Full-attention architectures (VGGT, DA3) and Point3R scale linearly with sequence length, with Point3R running out of memory beyond ~ 600 frames on a 32 GB GPU. FILT3R maintains effectively the same constant-memory footprint as CUT3R while TTT3R nearly doubles memory due to cached attention maps for attention-map-based gating.

4.7 Analysis

To understand why FILT3R improves long-horizon stability, we analyze its induced update dynamics on long TUM-RGBD sequences. FILT3R behaves as an

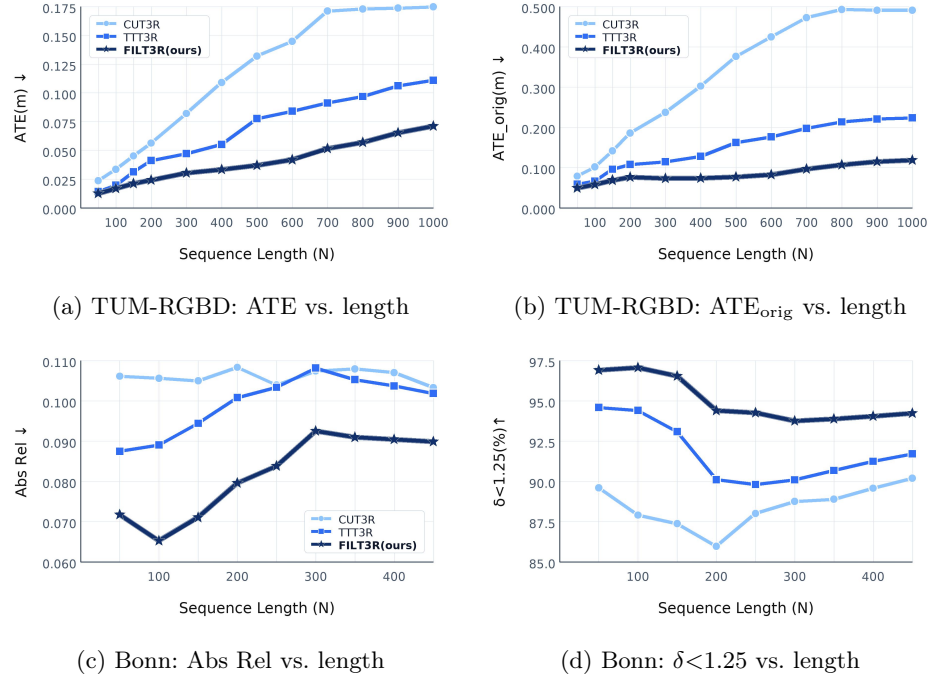


Fig. 4: Long-horizon metrics vs. sequence length. Top (a, b): Camera pose on TUM-RGBD (50–1000 frames). FILT3R’s drift grows more slowly. Bottom (c, d): Metric scale video depth on Bonn (50–500 frames). FILT3R consistently mitigates drift and improves over the baselines as the sequence progresses.

Table 4: Short-horizon depth (controlled streaming comparison). All methods share identical weights; only the update rule differs.

Align.	Method	Sintel		Bonn		KITTI	
		AbsRel↓	$\delta < 1.25$ ↑	AbsRel↓	$\delta < 1.25$ ↑	AbsRel↓	$\delta < 1.25$ ↑
Scale	CUT3R	0.421	47.9	0.078	93.7	0.118	88.1
	TTT3R	0.405	48.9	0.069	95.4	0.114	90.4
	FILT3R (ours)	0.407	54.5	0.061	97.0	0.110	91.0
Metric	CUT3R	1.029	23.8	0.103	88.5	0.122	85.5
	TTT3R	0.977	24.5	0.090	94.2	0.110	89.1
	FILT3R (ours)	0.772	27.3	0.067	96.7	0.115	88.8

uncertainty-calibrated conservative updater: as confidence accumulates, propagated uncertainty contracts and the effective gain settles into a low-update regime, which reduces the applied update magnitude. This matches the error profile in Table 2: FILT3R substantially lowers ATE_{orig} while leaving short-horizon RPE nearly unchanged, indicating that its main benefit is not more

Table 5: Runtime and GPU memory (500 frames). Benchmark on NRGBD (512×384, warmup=2, 10 runs). **FILT3R (ours)** avoids attention-map caching, matching CUT3R’s footprint.

Method	Attn	FPS↑	Mem(MB)↓
CUT3R	–	25.27±.05	3503
TTT3R	✓	24.69±.05	6294
FILT3R (adpt. r_t)	✓	24.83±.04	6294
FILT3R (ours)	–	25.14±.04	3503

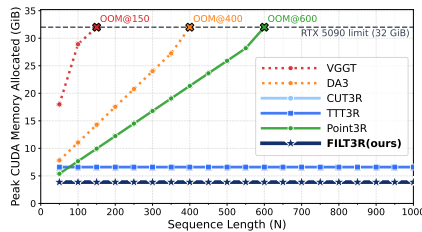


Fig. 5: Peak GPU mem. vs. frames. Full-attention methods (VGGT, DA3) and Point3R grow with length; CUT3R/FILT3R stay constant. FILT3R overlaps CUT3R, confirming negligible overhead.

Table 6: Ablation study of FILT3R components. All variants use identical frozen backbone weights and identical inference code; only the online update policy is changed. We report long-horizon pose on TUM-800 and long-horizon metric depth on Bonn-500. Lower is better (↓) except $\delta < 1.25$ (↑).

Variant	TUM-800 (pose)				Bonn-500 (metric depth)		
	ATE↓	ATE _{orig} ↓	RPE-t↓	RPE-r↓	AbsRel↓	$\delta < 1.25$ ↑	logRMSE↓
FILT3R (full)	0.057	0.107	0.009	0.362	0.089	94.4	0.148
Fixed-Q (fixed r)	0.100	0.229	0.009	0.393	0.099	91.9	0.155
No variance propagation (reset-P)	0.149	0.489	0.009	0.446	0.099	91.1	0.154
Fixed- β EMA ($\beta=0.05$, tuned)	0.049	0.078	0.010	0.658	0.093	93.5	0.152
No EMA normalization for drift	0.058	0.109	0.010	0.367	0.091	94.1	0.150
Adaptive measurement noise (r_t)	0.074	0.148	0.009	0.372	0.093	93.9	0.151

aggressive correction at transition frames, but less persistent overwrite of the latent state and therefore slower cumulative drift. The adaptive process-noise term still matters because it temporarily relaxes this conservative regime on difficult frames, allowing the model to remain responsive without reverting to continual high-gain updates; consistent with this interpretation, removing uncertainty propagation in Table 6 substantially degrades long-horizon performance. Detailed transition-level statistics are provided in Appendix 9.

4.8 Ablations

All variants in Table 6 share identical frozen backbone weights and identical inference code; we only change the *online state update*. FILT3R’s update is fully determined by the gain $\beta_t = \mathbf{k}_t$ in Eq. (5), which in turn depends on (i) the process noise \mathbf{q}_t (Eq. (7)), (ii) the measurement noise r (Eq. (4)), and (iii) whether uncertainty is *propagated* through the variance recursion (Eqs. (3)–(6)). The ablations isolate each of these design choices.

(i) *Adaptive process noise is necessary for targeted adaptation.* **Fixed-Q** replaces the drift-driven \mathbf{q}_t with a constant. This removes the ability to temporarily increase the update strength during genuine motion bursts or scene change. As a result, long-horizon drift grows substantially (e.g., ATE_{orig} increases from 0.107 to 0.229), and depth accuracy also degrades (AbsRel 0.089 \rightarrow 0.099). This indicates that adaptivity should enter through the *process model* rather than a fixed gate.

(ii) *Variance propagation enables confidence accumulation.* **No variance propagation (reset-P)** keeps the same gain formula but discards the recursive uncertainty update. Without accumulated confidence, the gain cannot systematically shrink in stable intervals, so the model keeps injecting per-frame measurement noise into the state, leading to severe long-horizon drift (ATE_{orig} 0.107 \rightarrow 0.489) and worse depth (AbsRel 0.089 \rightarrow 0.099). This confirms that the Kalman-style *propagation* (not just the functional form of the gain) is important.

(iii) *A tuned fixed-gain EMA can reduce ATE, but it harms local motion and depth.* **Fixed- β EMA** uses a constant update $\mathbf{s}_t = (1 - \beta)\mathbf{s}_{t-1} + \beta\tilde{\mathbf{s}}_t$ with $\beta = 0.05$ tuned on a development set. Interestingly, this can yield *lower* trajectory ATE on TUM-800 (0.049 vs. 0.057) and also improve ATE_{orig} (0.078 vs. 0.107), suggesting that a conservative fixed update can suppress some global drift. However, it does so by uniformly damping updates, which noticeably degrades *local* relative motion: rotation error increases sharply (RPE-r 0.362 \rightarrow 0.658). At the same time, depth quality is still worse than FILT3R. Overall, fixed- β behaves like a *global low-pass filter*: it can reduce drift under some metrics, but it cannot simultaneously preserve accurate short-term motion and maintain depth quality across long rollouts. This highlights the need for *uncertainty-aware* and *transition-aware* gains rather than a single fixed forgetting rate.

(iv) *EMA normalization is a stabilizer but not the dominant factor here.* **No EMA normalization** removes the running baseline $\hat{\Delta}_t$ in Eq. (9). On these benchmarks, drift magnitudes are already relatively well-scaled, so the effect is modest (e.g., ATE_{orig} 0.107 \rightarrow 0.109; AbsRel 0.089 \rightarrow 0.091). We keep EMA normalization as a robust default because it mitigates early/late scale shifts and reduces gain jitter when drift statistics vary across scenes and sequences.

(v) *Adaptive measurement noise hurts long-horizon stability and adds overhead.* **Adaptive r_t** replaces the fixed scalar r with a per-token measurement noise estimated from attention statistics, following the intuition that tokens attending strongly to image evidence should be trusted more (lower $r_{t,i}$). However, this variant degrades long-horizon performance compared to the full model: ATE_{orig} increases from 0.107 to 0.148 and ATE from 0.057 to 0.074, while depth also worsens (AbsRel 0.089 \rightarrow 0.093, $\delta < 1.25$ 94.4 \rightarrow 93.9). We believe the reason is that attention-aligned novelty is correlated with temporal drift: during scene transitions, both \mathbf{q}_t increases (from large drift) and $r_{t,i}$ decreases (from high attention to novel content), causing the gain to spike more aggressively than either

signal alone would warrant. This co-excitation amplifies updates precisely when stability matters most, undermining the filter’s conservative accumulation of confidence. Since adaptive r_t additionally requires caching attention maps—nearly doubling GPU memory to match attention-based gating baselines (Tab. 5)—we favor the simpler and more stable design: a fixed scalar r as a measurement-noise anchor, with all adaptivity concentrated in the process noise \mathbf{q}_t .

5 Conclusion

We introduced FILT3R, a principled, training-free solution to the long-horizon drift and catastrophic forgetting that typically degrade streaming 3D reconstruction. By casting recurrent token updates as an adaptive Kalman filtering problem, FILT3R explicitly propagates per-token uncertainty to dynamically balance historical memory retention with fast adaptation. Crucially, this uncertainty-aware state fusion acts as a plug-and-play stabilizer. Relying solely on internal temporal drift to estimate process noise—anchored by a single, fixed measurement noise scalar—it unifies and outperforms prior heuristic update rules without requiring any retraining. Our extensive evaluations across video depth, camera pose, and 3D reconstruction demonstrate that FILT3R significantly extends the effective memory horizon, paving the way for highly stable, continuous, and long-form online scene understanding.

Appendix Index

This appendix is organized as follows.

A. Method, theoretical analysis, and comparison with fixed-EMA smoothing	17
A.1 Growth of the effective memory horizon	18
A.2 Implemented gain floor	22
A.3 Distinguishing FILT3R from fixed-EMA smoothing	22
B. Why periodic hard resets are not sufficient	26
C. Evaluation protocol and reproducibility	27
D. Additional long-horizon depth results on KITTI	31
E. Complete short-horizon tables	32
F. Hyperparameter details	34
G. Additional qualitative evidence of long-horizon stability	34

A Method, theoretical analysis, and comparison with fixed-EMA smoothing

Update rule recap. FILT3R modifies only the recurrent state-update rule, while backbone weights, decoder weights, and all other aspects of recurrent inference remain unchanged. Specifically, let $\tilde{s}_{t,i}$ denote the decoder’s candidate token for the i -th token at frame t , let $p_{t,i}$ denote the propagated per-token variance, and let r be the fixed scalar measurement noise shared across all tokens and experiments. FILT3R computes a normalized drift score from consecutive candidate states and maps it to per-token process noise via a sigmoid gate:

$$\Delta_{t,i} = \|\tilde{s}_{t,i} - \tilde{s}_{t-1,i}\|_2, \quad \hat{\Delta}_t = (1 - \lambda_\Delta)\hat{\Delta}_{t-1} + \lambda_\Delta\bar{\Delta}_t, \quad \bar{\Delta}_t = \frac{1}{N} \sum_i \Delta_{t,i}, \quad (11)$$

$$g_{t,i} = \Delta_{t,i}/\hat{\Delta}_t, \quad q_{t,i} = q_{\min} + (q_{\max} - q_{\min})\sigma(\alpha_q(g_{t,i} - \tau_q)). \quad (12)$$

where $\sigma(\cdot)$ denotes the sigmoid. The resulting process noise $q_{t,i}$ enters the scalar Kalman-style update:

$$p_{t,i}^- = p_{t-1,i} + q_{t,i}, \quad k_{t,i} = \frac{p_{t,i}^-}{p_{t,i}^- + r}, \quad (13)$$

$$s_{t,i} = (1 - k_{t,i})s_{t-1,i} + k_{t,i}\tilde{s}_{t,i}, \quad p_{t,i} = (1 - k_{t,i})^2 p_{t,i}^- + k_{t,i}^2 r. \quad (14)$$

The complete per-frame procedure is summarized in Algorithm 1.

The chain of effects is as follows: large drift raises $q_{t,i}$, larger $q_{t,i}$ raises the predicted variance $p_{t,i}^-$, larger $p_{t,i}^-$ raises the gain $k_{t,i}$, and a larger gain makes the state move more aggressively toward the new candidate. Conversely, if the stream remains stable for many frames, then $q_{t,i}$ stays small and the Joseph update in Eq. (14) contracts the posterior variance $p_{t,i}$, which reduces future gains and makes the latent state increasingly conservative. This is beneficial because the decoder’s candidate \tilde{s}_t is a noisy single-frame estimate: in stable regions, the accumulated state is a more reliable scene representation, and conservative updates preserve this advantage.

This is the key distinction from TTT3R. TTT3R is also adaptive, but its gate is computed directly from current-frame cues (e.g., attention/change statistics) and does not maintain a propagated covariance state. FILT3R separates these two roles: $q_{t,i}$ provides frame-dependent adaptivity, while $p_{t,i}$ carries forward accumulated confidence. As a result, FILT3R’s gain depends not only on what is happening in the current frame, but also on how much consistent evidence has already been accumulated across the preceding history.

For numerical stability, a small ε is added to the denominators of the gain and normalized drift computations, the gain is clamped to $[k_{\min}, k_{\max}]$, and the EMA drift baseline is clamped to a floor Δ_{floor} . The additional state beyond the baseline consists of one N -dimensional variance vector, one scalar EMA baseline per stream, and one buffer storing the previous candidate state.

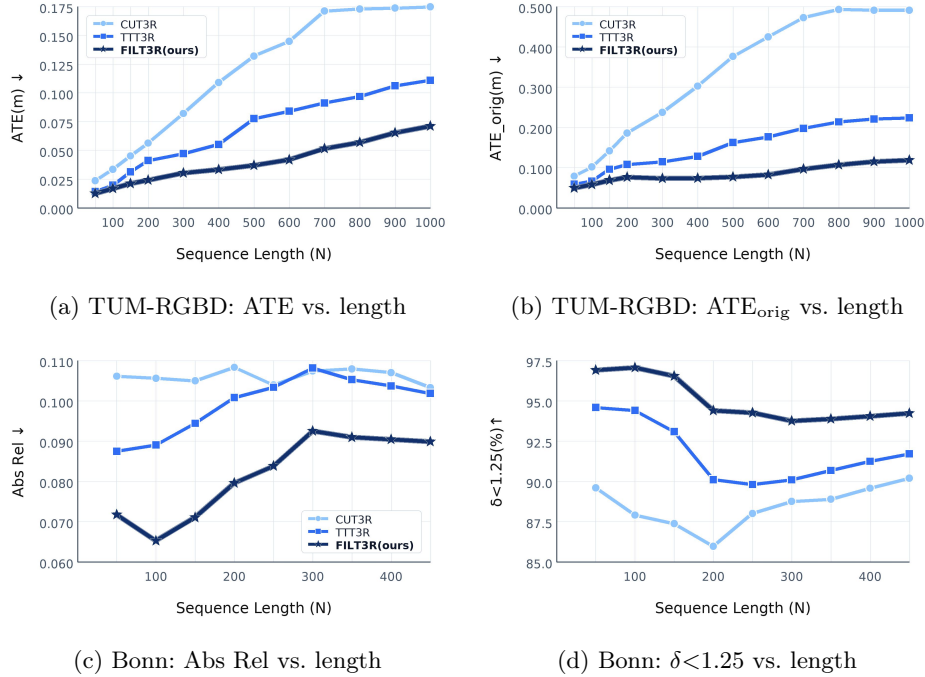


Fig. 6: FILT3R slows long-horizon error growth. Across both camera pose and metric-scale depth, FILT3R’s errors grow more slowly than those of overwrite (CUT3R) and heuristic gating (TTT3R) as the evaluated prefix length increases. This is the central empirical pattern that the remainder of the appendix explains.

Notation and first-frame handling. Notation follows the main paper. In Sec. A.1, we write $\beta_{t,i} := k_{t,i}$ only to make the smoothing interpretation explicit; all other symbols are unchanged. On the first valid frame, the latent state is initialized by direct overwrite with the current candidate, the covariance is set to p_0 for every token, and the previous-candidate buffer is set to the current candidate state. The drift EMA is not preseeded separately: when the first temporal difference becomes available, its running value is initialized from that mean drift and then clamped to Δ_{floor} .

A.1 Growth of the effective memory horizon

The Kalman gain $k_{t,i}$ acts as a per-token update coefficient $\beta_{t,i} := k_{t,i} \in [0, 1]$, yielding a time-varying exponential smoothing:

$$s_{t,i} = (1 - \beta_{t,i})s_{t-1,i} + \beta_{t,i}\tilde{s}_{t,i}. \quad (15)$$

Algorithm 1 **FILT3R replaces only the latent-state update.** The recurrent architecture, decoder, and backbone checkpoint are otherwise identical to the baseline.

Require: Previous latent state \mathbf{s}_{t-1} , covariance \mathbf{p}_{t-1} , candidate state $\tilde{\mathbf{s}}_{t-1}$, and measurement noise r

- 1: Decode the current frame with the frozen streaming backbone to obtain candidate state $\tilde{\mathbf{s}}_t$.
 - 2: Compute temporal drift from $\tilde{\mathbf{s}}_t$ and $\tilde{\mathbf{s}}_{t-1}$; update the EMA drift baseline.
 - 3: Estimate per-token process noise \mathbf{q}_t with Eq. (7).
 - 4: Predict covariance: $\mathbf{p}_t^- = \mathbf{p}_{t-1} + \mathbf{q}_t$.
 - 5: Compute Kalman gain: $\mathbf{k}_t = \mathbf{p}_t^- / (\mathbf{p}_t^- + r)$.
 - 6: Update latent state: $\mathbf{s}_t = (1 - \mathbf{k}_t) \odot \mathbf{s}_{t-1} + \mathbf{k}_t \odot \tilde{\mathbf{s}}_t$.
 - 7: Update covariance with the scalar Joseph recursion (Eq. 14).
 - 8: Store $\tilde{\mathbf{s}}_t$ and \mathbf{p}_t for the next frame.
-

Unrolling this recursion gives a weighted history of past candidates:

$$s_{t,i} = \left(\prod_{u=1}^t (1 - \beta_{u,i}) \right) s_{0,i} + \sum_{\tau=1}^t \left(\beta_{\tau,i} \prod_{u=\tau+1}^t (1 - \beta_{u,i}) \right) \tilde{s}_{\tau,i}. \quad (16)$$

A constant gain $\beta_{t,i} \equiv \beta$ gives a fixed exponential memory horizon. If $\beta_{t,i}$ decreases over time, older candidates decay more slowly and the effective memory horizon expands.

We can distinguish TTT3R and FILT3R more clearly. Both methods are adaptive in the broad sense that their update coefficients can change with time. The difference is *how* that change is generated. TTT3R changes its gate from current cues, but it does not propagate a covariance state whose contraction makes the gate depend on accumulated confidence. FILT3R does. Its gain at time t depends both on the current process-noise estimate $q_{t,i}$ and on the recursively propagated uncertainty $p_{t-1,i}$. Therefore the same amount of instantaneous drift can lead to a smaller update after a long stable stretch than it would immediately after a transition.

The following proposition isolates this mechanism in the cleanest possible setting. It is intentionally idealized: the scene is static, $q = 0$, and no implementation clamps are applied.

Proposition 1 (Static scenes yield naturally shrinking gains). *Consider a scalar token in a static regime: the true latent is constant s^* , measurements are $\tilde{s}_t = s^* + v_t$ with $v_t \sim \mathcal{N}(0, r)$, and process noise is zero ($q = 0$). Then the Kalman recursion gives*

$$p_t = \frac{1}{\frac{1}{p_0} + \frac{t}{r}} = \mathcal{O}\left(\frac{1}{t}\right), \quad k_t = \frac{p_{t-1}}{p_{t-1} + r} = \frac{1}{t + r/p_0}. \quad (17)$$

Proof. With $q = 0$, the prediction step is $p_t^- = p_{t-1}$ and $k_t = p_t^- / (p_t^- + r)$. The Joseph update (Eq. 14) gives

$$\begin{aligned} p_t &= (1 - k_t)^2 p_t^- + k_t^2 r = \frac{r^2}{(p_t^- + r)^2} p_t^- + \frac{(p_t^-)^2}{(p_t^- + r)^2} r \\ &= \frac{p_t^- r (r + p_t^-)}{(p_t^- + r)^2} = \frac{p_t^- r}{p_t^- + r} = (1 - k_t) p_t^-. \end{aligned} \quad (18)$$

Therefore $1/p_t = 1/p_{t-1} + 1/r$, which telescopes to $1/p_t = 1/p_0 + t/r$. Substituting into $k_t = p_{t-1}/(p_{t-1} + r)$ yields Eq. (17).

Proposition 1 shows that, under repeated consistent observations, precision accumulates linearly, the posterior variance shrinks as $\mathcal{O}(1/t)$, and the gain shrinks at the same order. The filter therefore behaves like an average over an ever longer history rather than an update with a fixed forgetting rate. Overwrite (CUT3R, $k_t \equiv 1$) lacks this mechanism, and an instantaneous gate such as TTT3R may vary from frame to frame but has no propagated covariance recursion that forces this specific gain decay as confidence accumulates.

The next proposition considers a different regime, constant $q > 0$. Unlike Proposition 1, which isolates the idealized zero-process-noise mechanism, this result characterizes the finite steady-state operating point of the same scalar recursion. In Sec. A.2 we use it to interpret the implemented gain floor when $q_{t,i}$ settles near q_{\min} .

Proposition 2 (Steady-state gain vs. q/r). *For the scalar random-walk model with constant process noise $q > 0$ and measurement noise $r > 0$, the posterior variance converges to a unique positive steady state*

$$p^* = \frac{\sqrt{q^2 + 4qr} - q}{2}, \quad (19)$$

and the corresponding steady-state Kalman gain is

$$k^* = \frac{p^* + q}{p^* + q + r} = \frac{\sqrt{q^2 + 4qr} + q}{\sqrt{q^2 + 4qr} + q + 2r}. \quad (20)$$

Proof. At steady state the posterior variance satisfies $p_t = p_{t-1} = p^*$. We derive the fixed-point equation in three steps.

Step 1: Predicted variance. The prediction step gives $p^- = p^* + q$.

Step 2: Steady-state gain. The Kalman gain is $k^* = p^- / (p^- + r) = (p^* + q) / (p^* + q + r)$.

Step 3: Fixed-point equation. For the Kalman gain above, the Joseph form simplifies to $(1 - k^*) p^-$ (as shown in Eq. 18), giving the fixed-point condition

$$p^* = (1 - k^*) p^- = \frac{r}{p^- + r} \cdot p^- = \frac{r(p^* + q)}{p^* + q + r}.$$

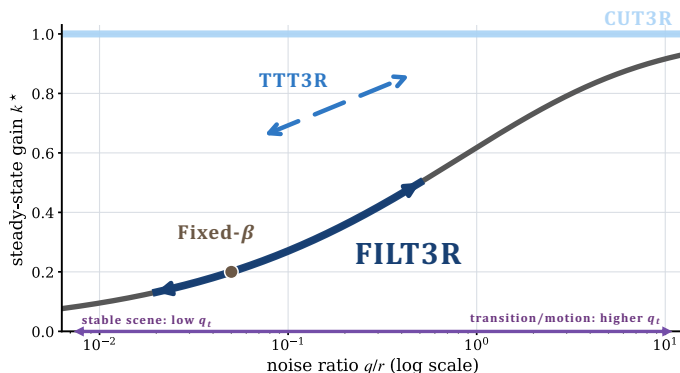


Fig. 7: How different update rules relate to the gain curve. With fixed r , the steady-state Kalman gain is determined by the noise ratio (q/r). Overwrite (CUT3R) corresponds to the limit ($k \rightarrow 1$). A fixed gate chooses one constant operating point. FILT3R adapts q_t and therefore moves along the curve, becoming conservative in stable regimes and reopening at transitions. TTT3R is also adaptive, but its gate is heuristic and based on current cues rather than propagated covariance, so it is shown schematically off the steady-state curve.

By cross-multiplying and expanding the left side, the $r p^*$ terms cancel, yielding the quadratic

$$(p^*)^2 + q p^* - qr = 0. \quad (21)$$

The quadratic formula gives Eq. (19). Substituting p^* back into $k^* = (p^* + q)/(p^* + q + r)$ and noting that $p^* + q = (q + \sqrt{q^2 + 4qr})/2$ yields Eq. (20). Finally, to show the convergence, write the scalar variance recursion as

$$p_t = f(p_{t-1}), \quad f(p) = \frac{r(p+q)}{p+q+r}.$$

For all $p \geq 0$,

$$f'(p) = \frac{r^2}{(p+q+r)^2} < 1,$$

so f is a contraction on $[0, \infty)$. Therefore the positive fixed point is unique and the recursion converges to it.

Proposition 2 gives the right interpretation of the adaptive process-noise term: with fixed r , the ratio q/r determines the operating point on the gain curve. A fixed gate chooses one point on this curve. TTT3R can still change its gate heuristically from frame to frame, but it does so without a propagated covariance state and therefore without the same confidence-accumulation mechanism. FILT3R combines both ingredients: q_t provides frame-dependent adaptivity, while p_t carries accumulated confidence across time.

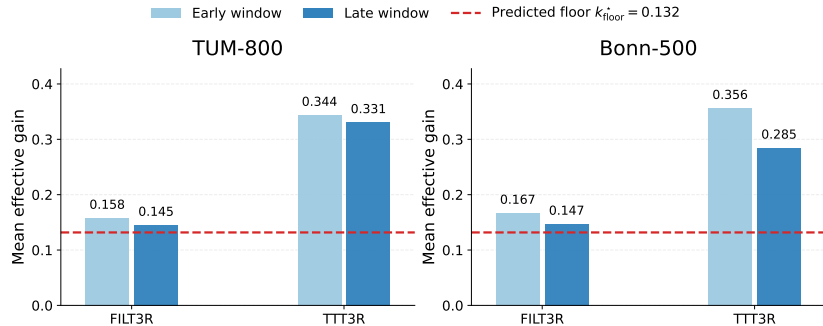


Fig. 8: The deployed filter settles near a finite gain floor rather than freezing completely. The dashed line marks the implementation-faithful prediction $k_{\text{floor}}^* \approx 0.132$ from Eq. (22). Here, the early and late windows denote the first and last 20% of frames of each analyzed sequence. Across both TUM-800 and Bonn-500, FILTER3R’s late-window mean gain remains only 0.013–0.015 above this floor, while TTT3R stays substantially more reactive. This is consistent with FILTER3R entering a conservative stable regime and reopening only when transition frames push q_t upward.

A.2 Implemented gain floor

If a token remains in a stable regime so that $q_{t,i} \approx q_{\min}$, Proposition 2 implies the unclamped steady-state gain

$$k_{\text{floor}}^* = \frac{\sqrt{q_{\min}^2 + 4q_{\min}r} + q_{\min}}{\sqrt{q_{\min}^2 + 4q_{\min}r} + q_{\min} + 2r}. \quad (22)$$

For the actual hyperparameters ($q_{\min} = 0.02$, $r = 1.0$), Eq. (22) gives $k_{\text{floor}}^* \approx 0.132$ before applying the clamp. The practical interpretation is therefore not that FILTER3R freezes completely, but that it settles into a substantially more conservative update regime while preserving responsiveness to scene change.

This distinction matters for interpretation. The idealized $\mathcal{O}(1/t)$ result explains why recursive uncertainty propagation expands the effective memory horizon relative to overwrite or fixed-gain updates. The implemented model inherits the same qualitative mechanism, but its asymptotic behavior is controlled by q_{\min} and $[k_{\min}, k_{\max}]$. Figure 8 shows that on long sequences, FILTER3R’s gain approaches the predicted floor, confirming that the update has converged to its stable-regime operating point.

A.3 Distinguishing FILTER3R from fixed-EMA smoothing

The central difference between FILTER3R and overwrite, heuristic gating, or fixed-EMA smoothing is that FILTER3R *propagates uncertainty*. This propagation allows the update to become increasingly conservative as evidence accumulates, while still reopening when elevated process noise signals a genuine scene transition.

Table 7: FILT3R versus fixed smoothing: ablations on TUM-800 and Bonn-500. Removing adaptive process noise or variance propagation weakens long-horizon stability. A tuned fixed- β EMA can suppress certain global drift metrics, but does so by uniformly damping all updates, which substantially degrades local rotation accuracy. No single constant coefficient matches FILT3R’s joint performance across long-horizon drift, local motion accuracy, and depth quality.

Variant	TUM-800 (pose)				Bonn-500 (metric depth)		
	ATE \downarrow	ATE _{orig} \downarrow	RPE-t \downarrow	RPE-r \downarrow	AbsRel \downarrow	$\delta < 1.25 \uparrow$	logRMSE \downarrow
FILT3R (full)	0.057	0.107	0.009	0.362	0.089	94.4	0.148
Fixed- Q (fixed r)	0.100	0.229	0.009	0.393	0.099	91.9	0.155
No variance propagation (reset- P)	0.149	0.489	0.009	0.446	0.099	91.1	0.154
Fixed- β EMA ($\beta=0.05$, tuned)	0.049	0.078	0.010	0.658	0.093	93.5	0.152
No EMA normalization for drift	0.058	0.109	0.010	0.367	0.091	94.1	0.150
Adaptive measurement noise (r_t)	0.074	0.148	0.009	0.372	0.093	93.9	0.151

FILT3R does not merely select a different constant for the gate; it changes the *dynamics* of the gate itself, making it time-dependent through propagated uncertainty.

A natural alternative hypothesis is that a globally conservative fixed EMA already explains the observed long-horizon gains. The fixed- β comparison in Table 6 reveals a more nuanced picture: very small fixed β can indeed suppress TUM-800 drift and even improve Bonn-500 Abs Rel, but at the cost of over-smoothing local motion. For instance, reading from the extended sweep in Figure 10, $\beta = 0.01$ reduces TUM-800 ATE_{orig} to 0.080 and Bonn-500 Abs Rel to 0.085, yet its TUM-800 RPE-r jumps to 1.91; even $\beta = 0.03$ yields RPE-r of 1.25. FILT3R therefore acts as a *selective* smoother: it contracts updates as evidence accumulates, but does not commit to a single forgetting rate for the entire stream.

In our experiments, the fixed- β baseline in Table 6 uses the development-set choice $\beta = 0.05$. In the fixed-EMA development sweep, β is selected by minimizing the sum of camera and depth metrics for TUM-200 and Bonn-150. The longer-horizon test benchmarks in Figure 10 were not used in that choice.

Exact definitions of the ablations. *Fixed-Q* replaces Eq. (7) with a stream-independent constant $q_{t,i} \equiv \bar{q}$ while keeping variance propagation and fixed r . The ablation defaults to $\bar{q} = \frac{1}{2}(q_{\min} + q_{\max}) = 0.26$ ($q_{\min} = 0.02$, $q_{\max} = 0.5$). *No variance propagation (reset-P)* resets $p_{t-1,i}$ to the initialization value before each update, so the gain uses the same functional form but cannot accumulate confidence across frames. *Fixed- β EMA* removes the Kalman variance recursion and sets $k_{t,i} \equiv \beta$ for all tokens and frames. *No EMA normalization* feeds raw drift magnitudes into the same sigmoid gate instead of the normalized score $g_{t,i}$. *Adaptive measurement noise* replaces the scalar r with token-wise $r_{t,i}$ estimated from normalized attention entropy while leaving the rest of the update unchanged. For the reported ablation, let $a_{t,i,j}$ denote the absolute aggregated cross-attention from state token i to image token j in the first cross-attention

layer, let

$$p_{t,i,j} = \frac{a_{t,i,j}}{\sum_j a_{t,i,j} + \varepsilon}, \quad H_{t,i} = -\frac{\sum_j p_{t,i,j} \log p_{t,i,j}}{\log K + \varepsilon},$$

where K is the number of image tokens, and let \hat{H}_t be the EMA of the sequence-mean entropy with update rate 0.05. The ablation then uses

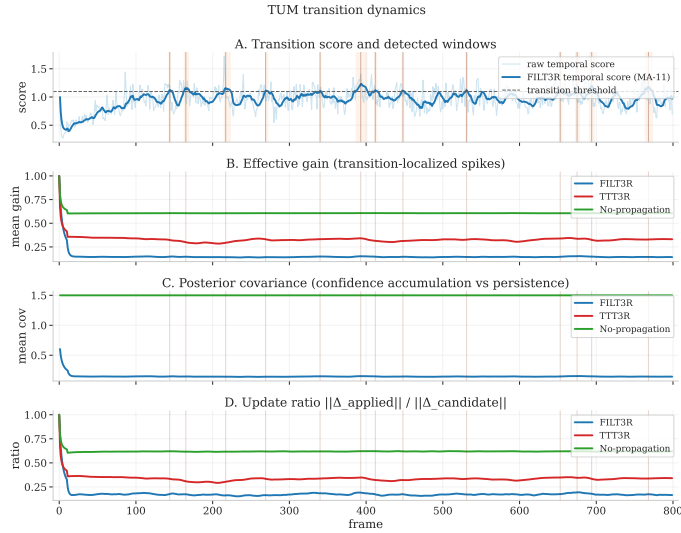
$$r_{t,i} = r_{\min} + r_{\text{scale}} \sigma\left(\alpha_r (H_{t,i}/\hat{H}_t - \tau_r)\right),$$

with $r_{\min} = 1.0$, $r_{\text{scale}} = 1.0$, $\alpha_r = 8.0$, and $\tau_r = 1.0$. The entropy signal is taken from the first cross-attention layer in all reported adaptive- r_t runs.

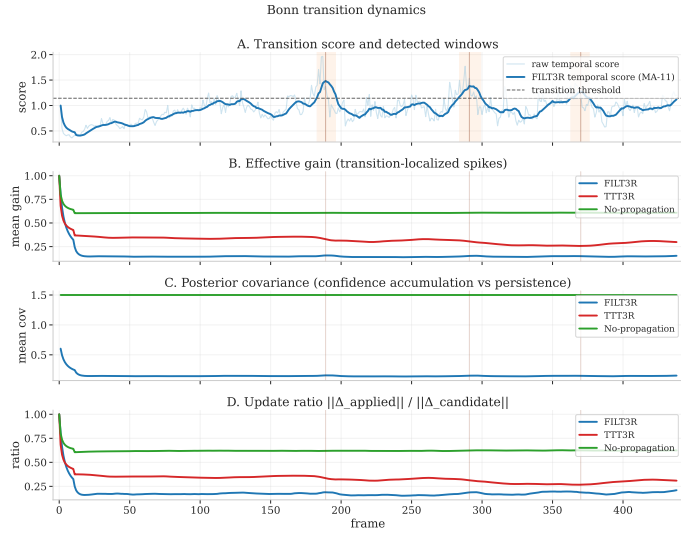
Diagnostic conventions used in Figures 8 and 9. The gain-floor summary in Figure 8 uses the first and last 20% of frames as the early and late windows. For the transition timelines in Figure 9, the *transition score* is the per-frame mean normalized drift $\bar{g}_t = \frac{1}{N} \sum_i g_{t,i}$ from Eq. (7). The plotted score is an MA-11 curve, meaning a trailing moving average over the previous 11 frames (including frame t). The *transition threshold* is the 90th percentile of this smoothed FILT3R score, and detected transition windows are contiguous regions above that threshold. *Effective gain* denotes the per-frame mean of the applied per-token gain $k_{t,i}$ after clamping, *posterior covariance* denotes the per-frame mean of the post-update variance $p_{t,i}$, and the *update ratio* is

$$\rho_t = \frac{\frac{1}{N} \sum_i \|s_{t,i} - s_{t-1,i}\|_2}{\frac{1}{N} \sum_i \|\tilde{s}_{t,i} - s_{t-1,i}\|_2},$$

that is, the mean applied update magnitude divided by the mean candidate-update magnitude.



(a) TUM-800 transition timeline



(b) Bonn-500 transition timeline

Fig. 9: FILT3R contracts updates in stable regimes and reopens at transitions. Panel A plots the per-frame mean temporal score \bar{g}_t together with its MA-11 smoothing, the 90th-percentile transition threshold, and the detected above-threshold windows. Panels B–D report the corresponding mean effective gain, mean posterior covariance, and update ratio ρ_t . Detected transition windows raise process noise, while propagated covariance keeps FILT3R in a substantially lower-update regime than both TTT3R and the no-propagation ablation. This behavior provides the mechanistic explanation for the slower error growth observed in Figure 4.

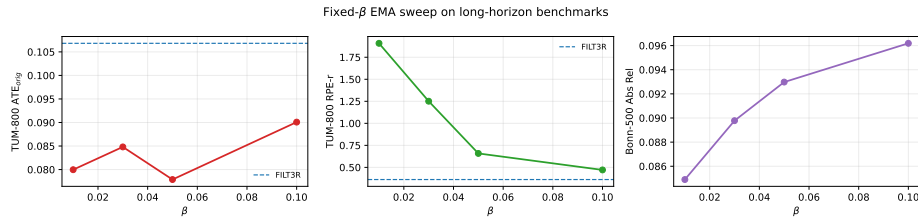


Fig. 10: Extended long-horizon fixed- β sweep. Very small fixed EMA coefficients can outperform FILT3R on individual long-horizon metrics, but only by globally over-smoothing the stream: the same settings that reduce ATE_{orig} or improve depth also produce substantially elevated TUM-800 RPE-r. FILT3R occupies a stronger operating region because it does not commit to a single forgetting rate for the entire rollout.

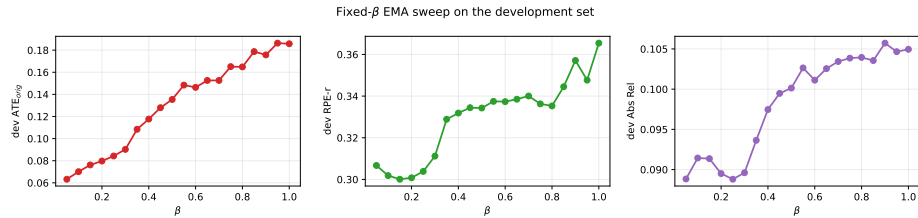


Fig. 11: Development-set fixed- β sweep. This sweep provides context for representative fixed-EMA operating points and shows the development-set optimum at $\beta = 0.05$ under the explicit objective above. The more informative comparison is the long-horizon sweep above: a fixed gate can be tuned toward one regime, yet it remains globally conservative rather than transition-aware.

B Why periodic hard resets are not sufficient

An alternative strategy for managing long-horizon drift is to periodically reset the recurrent state. We compare against the periodic hard-reset baseline used in the official TTT3R evaluation setup: the recurrent state is reinitialized every 100 frames while the frozen backbone and evaluator settings remain unchanged. At each reset, the persistent state and local memory return to their start-of-sequence values and the temporal buffers are cleared. While resets can reduce within-segment drift, they also discard accumulated scene context and risk introducing scale discontinuities at reset boundaries. The relevant criterion is whether resets preserve a coherent belief state over the full sequence, not merely whether they reduce within-segment drift.

Tables 8 and 9 address this question on TUM-RGBD (camera pose) and Bonn (depth), respectively. On TUM-RGBD (Table 8), TTT3R+Reset does improve locally aligned metrics such as ATE and RPE at moderate lengths, yet FILT3R remains substantially better on origin-aligned trajectory error at all evaluated horizons—for example, ATE_{orig} at TUM-800 is 0.107 for FILT3R versus 0.221 for TTT3R+Reset. On Bonn (Table 9), per-sequence scale alignment

Table 8: Resets improve within-segment metrics but fail to reduce cumulative drift. On TUM-RGBD, TTT3R+Reset improves certain locally aligned metrics, yet FILT3R remains substantially better on origin-aligned trajectory error, which directly exposes accumulated drift.

Method	TUM-400				TUM-600				TUM-800			
	ATE \downarrow	ATE $_{\text{orig}}\downarrow$	RPE-t \downarrow	RPE-r \downarrow	ATE \downarrow	ATE $_{\text{orig}}\downarrow$	RPE-t \downarrow	RPE-r \downarrow	ATE \downarrow	ATE $_{\text{orig}}\downarrow$	RPE-t \downarrow	RPE-r \downarrow
CUT3R	0.109	0.302	0.010	0.381	0.145	0.425	0.008	0.430	0.173	0.493	0.008	0.486
Point3R	0.119	0.179	0.028	0.640	0.133	0.205	0.026	0.912	0.157	0.241	0.024	1.127
TTT3R	0.055	0.128	0.010	0.328	0.084	0.176	0.009	0.365	0.097	0.214	0.009	0.387
TTT3R+Reset	0.047	0.140	0.008	0.308	0.059	0.181	0.007	0.331	0.077	0.221	0.007	0.338
FILT3R (ours)	0.033	0.074	0.009	0.305	0.042	0.082	0.009	0.332	0.057	0.107	0.009	0.362

Table 9: Reset depth comparison on Bonn. (a) Per-sequence scale alignment at 300, 400, and 500 frames shows that resets can help transiently. (b) Under metric-scale evaluation, however, FILT3R remains consistently stronger as the horizon grows, because it avoids the scale inconsistencies introduced at reset boundaries.

(a) Per-sequence scale (Bonn-300 / Bonn-400 / Bonn-500)

Method	Bonn-300			Bonn-400			Bonn-500		
	Abs Rel \downarrow	$\delta < 1.25 \uparrow$	log RMSE \downarrow	Abs Rel \downarrow	$\delta < 1.25 \uparrow$	log RMSE \downarrow	Abs Rel \downarrow	$\delta < 1.25 \uparrow$	log RMSE \downarrow
CUT3R	0.090	93.8	0.150	0.091	93.5	0.150	0.086	94.0	0.145
Point3R	0.083	94.7	0.149	0.083	94.6	0.147	0.081	94.8	0.145
TTT3R	0.079	95.0	0.142	0.078	95.1	0.139	0.075	95.3	0.136
TTT3R+Reset	0.085	94.3	0.147	0.082	94.5	0.142	0.081	94.8	0.141
FILT3R (ours)	0.080	95.1	0.143	0.078	95.3	0.140	0.076	95.4	0.138

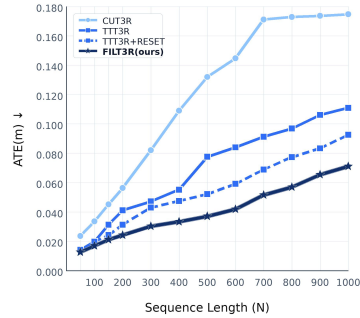
(b) Metric scale (Bonn-300 / Bonn-400 / Bonn-500)

Method	Bonn-300			Bonn-400			Bonn-500		
	Abs Rel \downarrow	$\delta < 1.25 \uparrow$	log RMSE \downarrow	Abs Rel \downarrow	$\delta < 1.25 \uparrow$	log RMSE \downarrow	Abs Rel \downarrow	$\delta < 1.25 \uparrow$	log RMSE \downarrow
CUT3R	0.107	88.7	0.162	0.107	89.6	0.161	0.101	90.6	0.156
Point3R	0.095	94.4	0.155	0.092	94.3	0.152	0.092	94.4	0.151
TTT3R	0.108	90.1	0.163	0.104	91.2	0.158	0.100	92.1	0.154
TTT3R+Reset	0.097	92.2	0.157	0.094	92.9	0.151	0.094	93.5	0.151
FILT3R (ours)	0.093	93.8	0.152	0.090	94.1	0.149	0.089	94.4	0.148

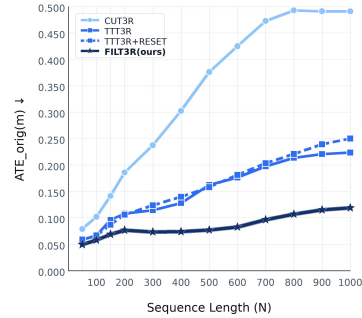
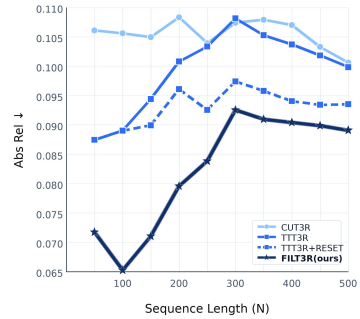
masks the issue: resets appear helpful at shorter horizons. Under metric-scale evaluation, however, FILT3R consistently outperforms the reset baseline as the horizon grows, because it avoids the scale discontinuities that resets introduce at segment boundaries. Figure 12 visualizes these trends as a function of sequence length, and Figure 13 shows representative qualitative failure cases where resets cause visible scale jumps.

C Evaluation protocol and reproducibility

Common setup. Unless stated otherwise, CUT3R, TTT3R, TTT3R+Reset, and FILT3R share the same frozen CUT3R checkpoint as in the main paper; only the online update rule differs. Point3R results are reproduced with the official codebase. Unless stated otherwise, every quantitative result in this appendix uses



(a) TUM-RGBD: ATE with reset

(b) TUM-RGBD: ATE_{orig} with reset

(c) Bonn: Abs Rel with reset

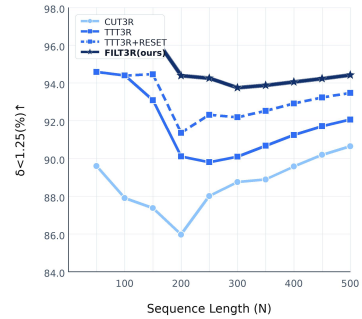
(d) Bonn: $\delta < 1.25$ with reset

Fig. 12: Resets improve short segments but not the persistent state. The reset baseline reduces locally aligned drift at moderate lengths, but its benefit diminishes as scale discontinuities accumulate across reset boundaries. FILT3R instead maintains a single continuously filtered state throughout the rollout.

the main FILT3R model with a single set of hyperparameters across all tasks. For each dataset, we extract frames at the native frame rate and truncate sequences to fixed prefix lengths; we refer to these as *prepared* sequences throughout.

Training-bound reference and evaluator settings. The public backbone checkpoint is `cut3r_512_dpt_4_64.pth`. This released CUT3R model is trained on *4-64 views*, so Table 10 reports evaluation lengths relative to the conservative 64-view upper training bound. The same table also collects the evaluator-side settings that materially affect the reported metrics: alignment mode for pose, scale handling for depth, valid-depth masks, and reconstruction crop / ICP settings.

Initialization, reset, and efficiency-benchmark details. On the first valid frame of a stream, the state is updated by direct overwrite with the current candidate, the covariance is initialized uniformly to p_0 , and the previous-candidate buffer is

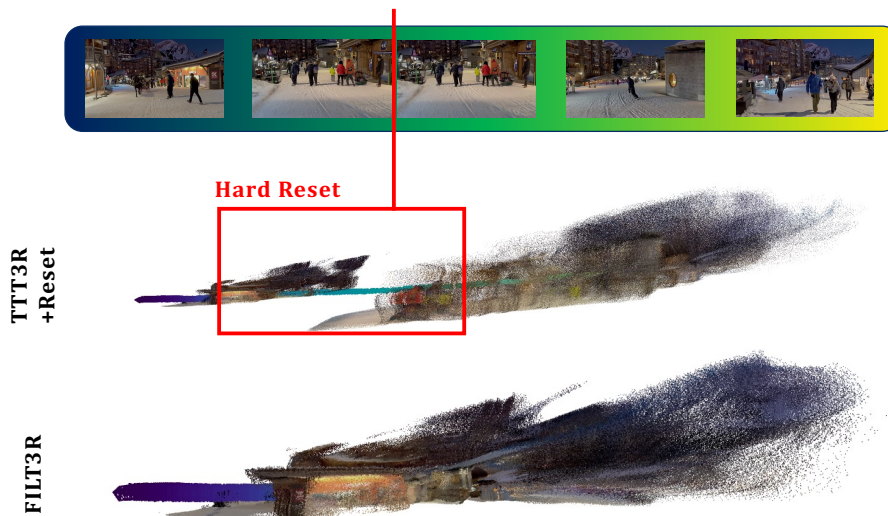


Fig. 13: Representative reset failure cases. Resetting discards previously accumulated scene context, causing scale jumps near reset boundaries and inconsistent behavior on revisited regions. FILT3R avoids these artifacts by maintaining a continuously filtered latent state.

Table 10: Exact evaluator settings and relation to the released checkpoint’s training bound. The checkpoint tag and README specify a 4–64-view model; we therefore state how far each benchmark extends beyond the 64-view upper bound.

Benchmark	Training ref.	Prefix lengths	Prefix / 64	Evaluator details
TUM-RGBD pose	CUT3R 4-64 views	50-1000	0.78×-15.63×	ATE uses <code>align=True</code> , <code>correct_scale=True</code> ; ATE _{orig} uses <code>align_origin=True</code> ; RPE is evaluated at $\Delta=1$ frame with similarity alignment.
Bonn depth	CUT3R 4-64 views	50-500	0.78×-7.81×	Main long-horizon table uses metric scale; the reset comparison additionally reports per-sequence scale alignment. Valid pixels satisfy GT depth > 0 and $< 70\text{m}$; predictions are bicubically resized and averaged with valid-pixel weighting.
KITTI depth	CUT3R 4-64 views	300 / 400 / 500	4.69×-7.81×	Both metric-scale and per-sequence-scale metrics are reported. The evaluator keeps the dataset’s native depth range (<code>max_depth=None</code>) and uses the same valid-pixel-weighted aggregation.
7-Scenes recon	CUT3R 4-64 views	100 / 200 / 300 / 500 / 1000	1.56×-15.63×	Input size 512 with a 224-pixel center crop for point cloud optimization. With ICP applied to report Accuracy, Completeness, and Normal Consistency.
NRGBD recon	CUT3R 4-64 views	300 / 400 / 500	4.69×-7.81×	The same reconstruction evaluator is used on the nine prepared NRGBD scenes.

set to that same candidate. The drift EMA is initialized only when the first temporal difference is available and is then clamped to Δ_{floor} . For TTT3R+Reset, we follow the official 100-frame hard-reset setup: the persistent state and local memory are reinitialized to their start-of-sequence values and temporal buffers are cleared, with no interval tuning on the evaluation sets. For the runtime / memory benchmark in the main paper, the protocol is NRGBD at 500 frames and 512×384 resolution, with 2 warmup runs and 10 timed runs, on a single-RTX 5090 32GB GPU.

Long-horizon camera pose on TUM-RGBD. Following [4], we evaluate eight prepared TUM-dynamics sequences:

- `freiburg3_sitting_{halfsphere,rpy,static,xyz}`
- `freiburg3_walking_{halfsphere,rpy,static,xyz}`.

For each prepared prefix length in $\{50, 100, 150, 200, 300, 400, 500, 600, 700, 800, 900, 1000\}$, we evaluate the full prefix and average metrics across the eight sequences. ATE is computed with global similarity alignment via `evo` package; ATE_{orig} uses origin alignment only to expose accumulated drift; RPE is computed at $\Delta = 1$ frame.

Long-horizon video depth on Bonn. Following [4], we evaluate the five long Bonn sequences `balloon2`, `crowd2`, `crowd3`, `person_tracking2`, and `synchronous`. Prepared prefix lengths are $\{50, 100, 150, 200, 250, 300, 350, 400, 450, 500\}$. The main-paper long-horizon depth table uses metric-scale evaluation; the reset table additionally reports per-sequence scale alignment. Depth metrics are aggregated with valid-pixel weighting.

Long-horizon video depth on KITTI. Following [4], we additionally report both per-sequence-scale and metric-scale depth on prepared KITTI validation clips truncated to 300, 400, and 500 frames. Depth metrics are aggregated with valid-pixel weighting.

3D reconstruction. 7-Scenes evaluation uses the prepared scene set with the frame budgets used in the paper (100, 200, 300, 500, and 1000). For 7-Scenes, we subsample every 2nd frame (stride 2) for sequence lengths below 500 and use every frame (stride 1) for the length-1000 evaluation. NRGBD evaluation uses the nine prepared scenes `breakfast_room`, `complete_kitchen`, `green_room`, `grey_white_room`, `kitchen`, `morning_apartment`, `staircase`, `thin_geometry`, and `whiteroom`. The reconstruction setup uses resolution 512 as input with a 224-pixel center crop for the ICP algorithm. Metrics are Accuracy, Completeness, and Normal Consistency.

Short-horizon benchmarks. Following [4], short-horizon depth is evaluated on the prepared Sintel split (14 sequences), the Bonn dynamics set with standard length (110), and KITTI validation crops. The short-horizon reconstruction table uses 7-Scenes at 100 and 200 frames, which therefore use stride 2.

Model selection and freeze point. A single fixed set of FILT3R hyperparameters is used across all tasks. We do *not* deploy different hyperparameters for pose and depth. Unlike the fixed- β baseline in Sec. A, the final fixed- R FILT3R model was not selected by a post hoc sweep on the long-horizon test tables. No single hidden scalar objective was used for that final model; the goal was one shared operating point that remained competitive on both the pose and depth development sets. Candidate fixed- R configurations were screened once on the pose development

Table 11: Targeted perturbation check around the main configuration. These runs come from retained evaluation logs and are intended as a local sensitivity check rather than a dense robustness study. The nearby setting stays in the same qualitative regime across both pose and reconstruction.

(a) TUM-800 pose			
Variant	ATE↓	ATE _{orig} ↓	RPE-r↓
Ours	0.057	0.107	0.362
Gate variant ($q_{\max}=0.8, \tau_q=4.0$)	0.057	0.107	0.364

(b) 7-Scenes reconstruction at length 300			
Variant	Acc (mean)↓	Comp (mean)↓	NC (mean)↑
Ours	0.020	0.022	0.568
Gate variant ($q_{\max}=0.8, \tau_q=4.0$)	0.020	0.022	0.568

set (TUM-200) and on a held-out short-horizon depth development set, after which one shared configuration was frozen and reused for every result reported in the main paper and this appendix. The neighboring variant (higher-ceiling, later-opening gate) in Table 11 and the isolated long-horizon wins of smaller fixed- β values were observed only in retained evaluation runs after this freeze point and did not influence model choice. Table 11 therefore serves as a targeted local sensitivity check rather than a dense robustness study.

Per-sequence robustness statistics. The gains in the main tables are not driven by a single favorable sequence. Table 12 summarizes the per-sequence runs at the longest horizons for which outputs are available for all compared methods: TUM-800 for pose and Bonn-400 for metric depth. FILT3R wins all eight TUM sequences on ATE_{orig} and wins three of the five Bonn sequences on Abs Rel, while also achieving the best mean and worst-case depth errors.

D Additional long-horizon depth results on KITTI

Discussion. Under per-sequence scale alignment (Table 13a), FILT3R consistently outperforms both CUT3R and TTT3R across all KITTI horizons. Under metric-scale evaluation (Table 13b), however, TTT3R holds a small edge over FILT3R—for example, Abs Rel of 0.132 versus 0.134 at KITTI-500—while both remain substantially better than CUT3R. We hypothesize that this is related to KITTI’s predominantly forward-driving motion, which produces relatively steady temporal drift and thus a setting where TTT3R’s heuristic gate may already be well-calibrated. Even in this regime, the gap to FILT3R remains small (within 0.002 Abs Rel at KITTI-500), while FILT3R remains stronger whenever per-sequence scale alignment is available.

Table 12: Per-sequence robustness at long horizons. TUM-800 pose uses all eight prepared TUM-dynamics sequences. Bonn-400 metric depth uses the five long Bonn sequences, which is the longest horizon for which per-sequence outputs are available for all compared methods.

(a) TUM-800 pose							
Method	ATE _{orig} mean±std↓ worst↓ wins↑			RPE-r mean±std↓ worst↓ wins↑			
CUT3R	0.493 ± 0.318	1.137	0	0.486 ± 0.240	0.862	0	
TTT3R	0.214 ± 0.097	0.427	0	0.387 ± 0.158	0.588	0	
TTT3R+Reset	0.221 ± 0.060	0.290	0	0.338 ± 0.113	0.483	5	
FILT3R (ours)	0.107 ± 0.029	0.136	8	0.362 ± 0.148	0.581	3	

(b) Bonn-400 metric depth							
Method	Abs Rel mean±std↓ worst↓ wins↑			$\delta < 1.25$ mean±std↑ worst↑ wins↑			
CUT3R	0.111 ± 0.049	0.190	0	88.3 ± 12.7	64.1	1	
TTT3R	0.108 ± 0.053	0.196	0	90.3 ± 10.2	71.6	1	
TTT3R+Reset	0.097 ± 0.040	0.148	2	92.4 ± 6.5	82.1	1	
FILT3R (ours)	0.092 ± 0.035	0.139	3	93.8 ± 4.4	87.5	2	

Table 13: Long-horizon video depth on KITTI. (a) Per-sequence scale alignment and (b) metric-scale evaluation are both reported on prepared KITTI validation clips truncated to 300, 400, and 500 frames.

(a) Per-sequence scale (KITTI-300 / KITTI-400 / KITTI-500)									
Method	KITTI-300			KITTI-400			KITTI-500		
	Abs Rel↓	$\delta < 1.25$ ↑	log RMSE↓	Abs Rel↓	$\delta < 1.25$ ↑	log RMSE↓	Abs Rel↓	$\delta < 1.25$ ↑	log RMSE↓
CUT3R	0.122	87.5	0.165	0.127	86.9	0.170	0.130	86.5	0.175
TTT3R	0.111	90.3	0.152	0.115	89.7	0.159	0.118	89.2	0.165
FILT3R (ours)	0.108	91.1	0.149	0.112	90.2	0.156	0.116	89.6	0.162

(b) Metric scale (KITTI-300 / KITTI-400 / KITTI-500)									
Method	KITTI-300			KITTI-400			KITTI-500		
	Abs Rel↓	$\delta < 1.25$ ↑	log RMSE↓	Abs Rel↓	$\delta < 1.25$ ↑	log RMSE↓	Abs Rel↓	$\delta < 1.25$ ↑	log RMSE↓
CUT3R	0.133	83.8	0.179	0.143	82.0	0.187	0.151	80.3	0.194
TTT3R	0.117	88.6	0.161	0.125	87.3	0.169	0.132	86.5	0.176
FILT3R (ours)	0.119	88.6	0.161	0.127	87.3	0.169	0.134	86.2	0.177

E Complete short-horizon tables

Tables 14 and 15 present the full short-horizon comparisons for depth and reconstruction, respectively. These tables include optimization-based and full-attention baselines in addition to the streaming methods compared in the main paper.

On short-horizon depth (Table 14), FILT3R is the strongest streaming method on Sintel and Bonn under metric-scale evaluation and remains competitive on KITTI; under per-sequence scale alignment it is competitive across all three datasets.

Table 14: Video depth estimation on short sequences (full comparison). Both per-sequence scale and metric-scale results are shown. Rows marked with † are reproduced from prior work.

Alignment	Method	Type	Sintel		Bonn		KITTI	
			Abs Rel↓	$\delta < 1.25$ †	Abs Rel↓	$\delta < 1.25$ †	Abs Rel↓	$\delta < 1.25$ †
Per-seq. scale	DUSt3R-GA† [33]	Optim	0.656	45.2	0.155	83.3	0.144	81.3
	MASt3R-GA† [11]	Optim	0.641	43.9	0.252	70.1	0.183	74.5
	MonST3R-GA† [37]	Optim	0.378	55.8	0.067	96.3	0.168	74.4
	Easi3R† [3]	FA	0.377	55.9	0.059	97.0	0.102	91.2
	VGGT†	FA	0.287	66.1	0.055	97.1	0.070	96.5
	DA3 [13]	FA	0.278	70.3	0.052	97.2	0.045	98.0
	Spann3R† [29]	Stream	0.622	42.6	0.144	81.3	0.198	73.7
	Point3R†	Stream	0.452	48.9	0.060	96.0	0.136	84.2
	CUT3R†	Stream	0.421	47.9	0.078	93.7	0.118	88.1
	TTT3R†	Stream	0.405	48.9	0.069	95.4	0.114	90.4
	STREAM3R ^α † [10]	Stream	0.478	51.1	0.075	94.1	0.116	89.6
	StreamVGGT† [40]	Stream	0.323	65.7	0.059	97.2	0.173	72.1
	MUT3R†	Stream	0.451	48.6	0.070	96.2	0.116	88.3
	FILT3R (ours)	Stream	<u>0.407</u>	<u>54.5</u>	<u>0.061</u>	<u>97.0</u>	0.110	91.0
	Metric scale	MASt3R-GA†	Optim	1.022	14.3	0.272	70.6	0.467
DA3 [13]		FA	0.529	6.2	0.147	88.8	0.237	28.5
CUT3R†		Stream	1.029	23.8	0.103	88.5	0.122	85.5
Point3R†		Stream	0.777	17.1	0.137	94.7	0.191	73.8
TTT3R		Stream	0.977	24.5	0.090	94.2	0.110	89.1
STREAM3R ^α †		Stream	1.041	21.0	0.084	94.4	0.234	57.6
MUT3R†		Stream	0.820	25.2	0.086	96.0	0.125	85.8
FILT3R (ours)		Stream	0.772	27.3	0.067	96.7	<u>0.115</u>	88.8

Table 15: 3D reconstruction on 7-Scenes at short sequences (100 and 200 frames). Even near the training horizon, FILT3R is already competitive with or slightly better than prior streaming updates, though the gap is considerably smaller than in the long-horizon settings reported above.

Method	Length 100						Length 200					
	Acc↓		Comp↓		NC↑		Acc↓		Comp↓		NC↑	
	Mean	Med.										
CUT3R	0.033	0.018	0.022	0.005	0.592	0.644	0.089	0.053	0.048	0.017	0.566	0.600
TTT3R	0.020	0.008	0.016	0.004	0.596	0.649	0.028	0.015	0.023	0.005	0.582	0.627
FILT3R (ours)	0.017	0.006	0.017	0.004	0.595	0.648	0.019	0.008	0.022	0.004	0.584	0.629

Scope of the empirical claim. The short-horizon gains are smaller than the long-horizon ones, so our central empirical claim is long-horizon stabilization rather than universal dominance across all regimes.

F Hyperparameter details

Table 16 lists the complete set of hyperparameters used by FILT3R. These values are fixed across all tasks and benchmarks reported in both the main paper and this appendix. As discussed in Sec. A.2, the positive q_{\min} together with gain clamping implies that the deployed filter has a finite stable-regime gain floor rather than an asymptotically vanishing gain.

Table 16: FILT3R hyperparameters.

Symbol	Description	Value
p_0	Initial per-token variance	1.5
k_{\min}, k_{\max}	Kalman gain clamp bounds	0.01, 0.99
q_{\min}, q_{\max}	Process noise bounds	0.02, 0.5
α_q, τ_q	Process-noise sigmoid parameters	20, 3.0
r	Fixed measurement-noise scalar	1.0
λ_{Δ}	Drift EMA rate	0.05
Δ_{floor}	Drift EMA floor	0.01
ε	Numerical stability constant	10^{-6}

G Additional qualitative evidence of long-horizon stability

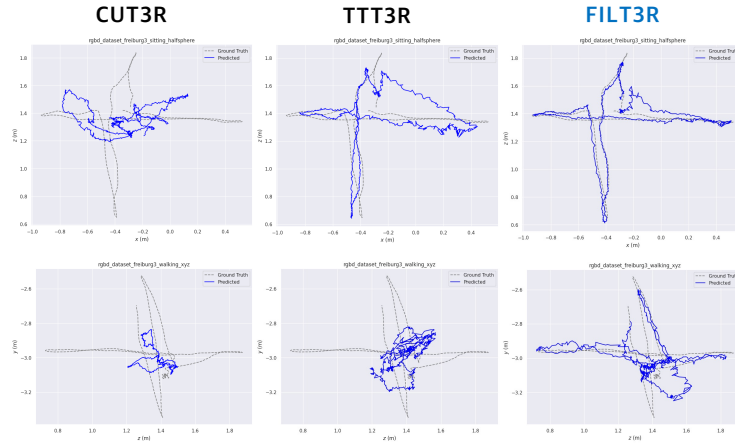


Fig. 14: TUM-RGBD trajectory visualizations. FILT3R stays closer to the ground-truth trajectory over long horizons than both the overwrite and heuristic-gating baselines, particularly after the rollout extends well beyond the training horizon.

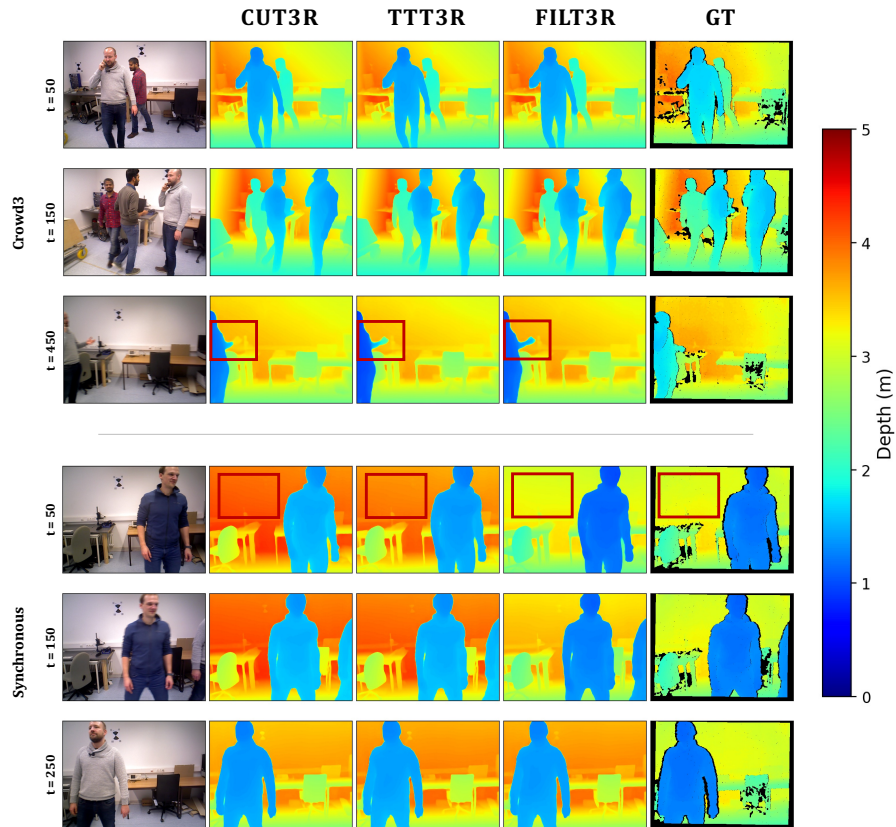


Fig. 15: Bonn depth prediction visualizations. FILT3R stays closer to the ground-truth depth over long horizons than both the overwrite and heuristic-gating baselines, producing more metric-aligned depth predictions with sharper detail.

References

1. Azinović, D., Martin-Brualla, R., Goldman, D.B., Nießner, M., Thies, J.: Neural rgb-d surface reconstruction. In: Proceedings of the IEEE/CVF Conference on Computer Vision and Pattern Recognition (CVPR). pp. 6290–6301 (June 2022)
2. Butler, D.J., Wulff, J., Stanley, G.B., Black, M.J.: A naturalistic open source movie for optical flow evaluation. In: Proceedings of the European Conference on Computer Vision (ECCV). pp. 611–625 (2012)
3. Chen, X., Chen, Y., Xiu, Y., Geiger, A., Chen, A.: Easi3R: Estimating disentangled motion from DUSt3R without training. In: Proceedings of the IEEE/CVF International Conference on Computer Vision (ICCV). pp. 9158–9168 (2025), https://openaccess.thecvf.com/content/ICCV2025/html/Chen_Easi3R_Estimating_Disentangled_Motion_from_DUST3R_Without_Training_ICCV_2025_paper.html
4. Chen, X., Chen, Y., Xiu, Y., Geiger, A., Chen, A.: TTT3R: 3d reconstruction as test-time training. In: International Conference on Learning Representations (ICLR) (2026), <https://openreview.net/forum?id=aMs6FtNaY5>
5. Deng, K., Ti, Z., Xu, J., Yang, J., Xie, J.: Vggt-long: Chunk it, loop it, align it – pushing vgg’s limits on kilometer-scale long rgb sequences (2025), <https://arxiv.org/abs/2507.16443>
6. Geiger, A., Lenz, P., Urtasun, R.: Are we ready for autonomous driving? the KITTI vision benchmark suite. In: Proceedings of the IEEE Conference on Computer Vision and Pattern Recognition (CVPR). pp. 3354–3361 (2012). <https://doi.org/10.1109/CVPR.2012.6248074>, <https://www.cvlibs.net/publications/Geiger2012CVPR.pdf>
7. Haarnoja, T., Zhou, A., Abbeel, P., Levine, S.: Backprop KF: Learning discriminative deterministic state estimators. In: Advances in Neural Information Processing Systems (NeurIPS). vol. 29 (2016), <https://proceedings.neurips.cc/paper/2016/hash/697e382cfd25b07a3e62275d3ee132b3-Abstract.html>
8. Kalman, R.E.: A new approach to linear filtering and prediction problems. *Journal of Basic Engineering* **82**(1), 35–45 (1960)
9. Krishnan, R.G., Shalit, U., Sontag, D.: Deep kalman filters (2015), <https://arxiv.org/abs/1511.05121>
10. Lan, Y., Luo, Y., Hong, F., Zhou, S., Chen, H., Lyu, Z., Dai, B., Yang, S., Loy, C.C., Pan, X.: SStream3R: Scalable sequential 3d reconstruction with causal transformer. In: International Conference on Learning Representations (ICLR) (2026), <https://openreview.net/forum?id=RTTYGeC2Io>, poster
11. Leroy, V., Cabon, Y., Revaud, J.: Grounding image matching in 3d with mast3r. In: Proceedings of the European Conference on Computer Vision (ECCV). pp. 71–91 (2024). https://doi.org/10.1007/978-3-031-73220-1_5, https://link.springer.com/chapter/10.1007/978-3-031-73220-1_5
12. Li, Z., Zhou, J., Wang, Y., Guo, H., Chang, W., Zhou, Y., Zhu, H., Chen, J., Shen, C., He, T.: Wint3r: Window-based streaming reconstruction with camera token pool. In: International Conference on Learning Representations (ICLR) (2026), <https://openreview.net/forum?id=PjviszIZf1>
13. Lin, H., Chen, S., Liew, J., Chen, D.Y., Li, Z., Zhao, Y., Shi, G., Feng, J., Kang, B., Peng, S., Guo, H., Zhou, X.: Depth anything 3: Recovering the visual space from any views. In: International Conference on Learning Representations (ICLR) (2026), <https://openreview.net/forum?id=yirunib818>
14. Liu, Y., Dong, S., Wang, S., Yin, Y., Yang, Y., Fan, Q., Chen, B.: Slam3r: Real-time dense scene reconstruction from monocular rgb videos. In: Proceedings of the

- IEEE/CVF Conference on Computer Vision and Pattern Recognition (CVPR). pp. 16651–16662 (2025)
15. Mehra, R.K.: On the identification of variances and adaptive kalman filtering. *IEEE Transactions on Automatic Control* **15**(2), 175–184 (1970). <https://doi.org/10.1109/TAC.1970.1099422>
 16. Murai, R., Dexheimer, E., Davison, A.J.: Mast3r-slam: Real-time dense slam with 3d reconstruction priors. In: *Proceedings of the IEEE/CVF Conference on Computer Vision and Pattern Recognition (CVPR)*. pp. 16695–16705 (2025)
 17. Palazzolo, E., Behley, J., Lottes, P., Giguère, P., Stachniss, C.: ReFusion: 3d reconstruction in dynamic environments for rgb-d cameras exploiting residuals. In: *IEEE/RSJ International Conference on Intelligent Robots and Systems (IROS)*. pp. 7855–7862 (2019). <https://doi.org/10.1109/IROS40897.2019.8967590>, <https://www.ipb.uni-bonn.de/pdfs/palazzolo2019iros.pdf>
 18. Sandström, E., Li, Y., Van Gool, L., Oswald, M.R.: Point-slam: Dense neural point cloud-based SLAM. In: *Proceedings of the IEEE/CVF International Conference on Computer Vision (ICCV)*. pp. 18433–18444 (2023)
 19. Shen, G., Deng, T., Qin, X., Wang, N., Wang, J., Wang, Y., Chen, Y., Wang, H., Wang, J.: Mut3r: Motion-aware updating transformer for dynamic 3d reconstruction (2025), <https://arxiv.org/abs/2512.03939>
 20. Shen, Y., Zhang, Z., Qu, Y., Zheng, X., Ji, J., Zhang, S., Cao, L.: Fastvggt: Fast visual geometry transformer. In: *International Conference on Learning Representations (ICLR)* (2026), <https://openreview.net/forum?id=as18Nj1Ime>
 21. Shotton, J., Glocker, B., Zach, C., Izadi, S., Criminisi, A., Fitzgibbon, A.: Scene coordinate regression forests for camera relocalization in rgb-d images. In: *Proceedings of the IEEE Conference on Computer Vision and Pattern Recognition (CVPR)*. pp. 2930–2937 (2013)
 22. Sturm, J., Engelhard, N., Endres, F., Burgard, W., Cremers, D.: A benchmark for the evaluation of rgb-d SLAM systems. In: *IEEE/RSJ International Conference on Intelligent Robots and Systems (IROS)*. pp. 573–580 (2012)
 23. Sucar, E., Liu, S., Ortiz, J., Davison, A.J.: iMAP: Implicit mapping and positioning in real-time. In: *Proceedings of the IEEE/CVF International Conference on Computer Vision (ICCV)*. pp. 6229–6238 (2021)
 24. Sun, Y., Wang, X., Liu, Z., Miller, J., Efros, A.A., Hardt, M.: Test-time training with self-supervision for generalization under distribution shifts. In: *Proceedings of the 37th International Conference on Machine Learning. Proceedings of Machine Learning Research*, vol. 119, pp. 9229–9248 (2020), <https://proceedings.mlr.press/v119/sun20b.html>
 25. Teed, Z., Deng, J.: Deepv2d: Video to depth with differentiable structure from motion. In: *International Conference on Learning Representations (ICLR)* (2020), <https://openreview.net/forum?id=HJe07RNKPr>
 26. Teed, Z., Deng, J.: Raft: Recurrent all-pairs field transforms for optical flow. In: *Proceedings of the European Conference on Computer Vision (ECCV)* (2020)
 27. Teed, Z., Deng, J.: Droid-slam: Deep visual slam for monocular, stereo, and rgb-d cameras. In: Ranzato, M., Beygelzimer, A., Dauphin, Y., Liang, P., Vaughan, J.W. (eds.) *Advances in Neural Information Processing Systems*. vol. 34, pp. 16558–16569. Curran Associates, Inc. (2021), https://proceedings.neurips.cc/paper_files/paper/2021/file/89fcd07f20b6785b92134bd6c1d0fa42-Paper.pdf
 28. Wang, D., Shelhamer, E., Liu, S., Olshausen, B., Darrell, T.: Tent: Fully test-time adaptation by entropy minimization. In: *International Conference on Learning Representations (ICLR)* (2021), <https://arxiv.org/abs/2006.10726>

29. Wang, H., Agapito, L.: 3d reconstruction with spatial memory. In: 2025 International Conference on 3D Vision (3DV). pp. 78–89 (2025). <https://doi.org/10.1109/3DV66043.2025.00013>
30. Wang, H., Wang, J., Agapito, L.: Co-SLAM: Joint coordinate and sparse parametric encodings for neural real-time SLAM. In: Proceedings of the IEEE/CVF Conference on Computer Vision and Pattern Recognition (CVPR). pp. 13293–13302 (2023)
31. Wang, J., Chen, M., Karaev, N., Vedaldi, A., Rupperecht, C., Novotny, D.: VGGT: Visual geometry grounded transformer. In: Proceedings of the IEEE/CVF Conference on Computer Vision and Pattern Recognition (CVPR). pp. 5294–5306 (2025)
32. Wang, Q., Zhang, Y., Holynski, A., Efros, A.A., Kanazawa, A.: Continuous 3d perception model with persistent state. In: Proceedings of the IEEE/CVF Conference on Computer Vision and Pattern Recognition (CVPR). pp. 10510–10522 (2025)
33. Wang, S., Leroy, V., Cabon, Y., Chidlovskii, B., Revaud, J.: Dust3r: Geometric 3d vision made easy. In: Proceedings of the IEEE/CVF Conference on Computer Vision and Pattern Recognition (CVPR). pp. 20697–20709 (2024)
34. Wang, Y., Zhou, J., Zhu, H., Chang, W., Zhou, Y., Li, Z., Chen, J., Pang, J., Shen, C., He, T.: π^3 : Permutation-equivariant visual geometry learning. In: International Conference on Learning Representations (ICLR) (2026), <https://openreview.net/forum?id=DTQIjngDta>, poster
35. Wu, Y., Zheng, W., Zhou, J., Lu, J.: Point3r: Streaming 3d reconstruction with explicit spatial pointer memory. In: Advances in Neural Information Processing Systems (NeurIPS) (2025), <https://openreview.net/forum?id=yk1iqV9Etr>
36. Yang, J., Sax, A., Liang, K.J., Henaff, M., Tang, H., Cao, A., Chai, J., Meier, F., Feiszli, M.: Fast3r: Towards 3d reconstruction of 1000+ images in one forward pass. In: Proceedings of the IEEE/CVF Conference on Computer Vision and Pattern Recognition (CVPR). pp. 21924–21935 (2025)
37. Zhang, J., Herrmann, C., Hur, J., Jampani, V., Darrell, T., Cole, F., Sun, D., Yang, M.H.: MonST3R: A simple approach for estimating geometry in the presence of motion. In: International Conference on Learning Representations (ICLR) (2025), <https://openreview.net/forum?id=1JpqxFgWCM>, spotlight
38. Zheng, Z., Xiang, X., Zhang, J.: TTSA3R: Training-free temporal-spatial adaptive persistent state for streaming 3d reconstruction (2026), <https://arxiv.org/abs/2601.22615>
39. Zhu, Z., Peng, S., Larsson, V., Xu, W., Bao, H., Cui, Z., Oswald, M.R., Pollefeys, M.: NICE-SLAM: Neural implicit scalable encoding for SLAM. In: Proceedings of the IEEE/CVF Conference on Computer Vision and Pattern Recognition (CVPR). pp. 12786–12796 (2022)
40. Zhuo, D., Zheng, W., Guo, J., Wu, Y., Zhou, J., Lu, J.: Streaming visual geometry transformer. In: International Conference on Learning Representations (ICLR) (2026), <https://openreview.net/forum?id=5APgTKsnx8>